Dynamics and energetics of the mammalian phosphatidylinositol transfer protein phospholipid exchange cycle

Aby Grabon[‡1], **Adam Orłowski**[§¶1], **Ashutosh Tripathi**[‡], **Joni Vuorio**[§‖], **Matti Javanainen**[§], **Tomasz Róg**[§‖], **Max Lönnfors**[‡], **Mark I. McDermott**[‡], **Garland Siebert**[‡], **Pentti Somerharju**[**], **Ilpo Vattulainen**[§‖‡‡2], and **Vytas A. Bankaitis**[‡§§¶¶3]

From the [‡]*Department of Molecular and Cellular Medicine, Texas A&M Health Science Center, College Station, Texas 77843, the* [§]*Laboratory of Physics, Tampere University of Technology, FI-33720 Tampere, Finland, the* [¶]*Department of Physics and Energy, University of Limerick, Limerick V94 T9PX, Ireland, the* [‖]*Department of Physics, University of Helsinki, P. O. Box 64, FI-00014 Helsinki, Finland, the* [**]*Department of Biochemistry and Developmental Biology, University of Helsinki, P. O. Box 63, FI-00014 Helsinki, Finland, the* [‡‡]*Department of Physics and Chemistry, MEMPHYS, Center for Biomembrane Physics, University of Southern Denmark, DK-5230 Odense, Denmark, and the Departments of* [§§]*Biochemistry and Biophysics and* [¶¶]*Chemistry, Texas A&M University, College Station, Texas 77843*

Edited by George M. Carman

Phosphatidylinositol-transfer proteins (PITPs) regulate phosphoinositide signaling in eukaryotic cells. The defining feature of PITPs is their ability to exchange phosphatidylinositol (PtdIns) molecules between membranes, and this property is central to PITP-mediated regulation of lipid signaling. However, the details of the PITP-mediated lipid exchange cycle remain entirely obscure. Here, all-atom molecular dynamics simulations of the mammalian StART-like PtdIns/phosphatidylcholine (PtdCho) transfer protein PITPα, both on membrane bilayers and in solvated systems, informed downstream biochemical analyses that tested key aspects of the hypotheses generated by the molecular dynamics simulations. These studies provided five key insights into the PITPα lipid exchange cycle: (i) interaction of PITPα with the membrane is spontaneous and mediated by four specific protein substructures; (ii) the ability of PITPα to initiate closure around the PtdCho ligand is accompanied by loss of flexibility of two helix/loop regions, as well as of the C-terminal helix; (iii) the energy barrier of phospholipid extraction from the membrane is lowered by a network of hydrogen bonds between the lipid molecule and PITPα; (iv) the trajectory of PtdIns or PtdCho into and through the lipid-binding pocket is chaperoned by sets of PITPα residues conserved throughout the StART-like PITP family; and (v) conformational transitions in the C-terminal helix have specific functional involvements in PtdIns transfer activity. Taken together, these findings provide the first mechanistic description of key aspects of the PITPα PtdIns/PtdCho exchange cycle and offer a rationale for the high conservation of particular sets of residues across evolutionarily distant members of the metazoan StART-like PITP family.

Phosphatidylinositol (PtdIns)[4] is a metabolic precursor of phosphoinositides, and these lipids function as critical intracellular chemical signals in eukaryotes. Although much effort is invested in understanding the enzymes that produce and consume phosphoinositides, fundamental aspects for how phosphoinositide production is regulated and physically organized define unappreciated gaps in our understanding of how inositol lipid signaling is prosecuted in cells. It is in those contexts that PtdIns transfer proteins (PITPs) command increasing interest as activities that functionally channel lipid metabolic information to dedicated and tightly integrated phosphoinositide signaling circuits. It is therefore no surprise that the biological importance of PITPs is on striking display in both uni- and multicellular organisms. Phenotypes associated with defects in individual PITPs include: (i) non-redundant functions of individual PITPs in channeling phosphoinositide signaling to Golgi/endosomal membrane trafficking, lipid droplet metabolism, and endosomal phosphatidylserine metabolism in yeast (1–4), (ii) collapse of "extreme" polarized plant membrane growth programs required for tissue organogenesis (5–7), (iii) defects in embryogenesis and retinal degeneration disease in both *Drosophila* and zebrafish (8–11), and (iv) neurodegenera-

[4] The abbreviations used are: PtdIns, phosphatidylinositol; PITP, phosphatidylinositol-transfer protein; MD, molecular dynamics; PtdCho, phosphatidylcholine; PL, phospholipid; RMSD, root mean square deviation; RMSF, root mean square fluctuation; PDB, Protein Data Bank; MDS, molecular dynamics simulation; PyrPtdCho, 1-palmitoyl-2-decapyrenyl-*sn*-glycero-3-phosphocholine; PyrPtdIns, 1-palmitoyl-2-decapyrenyl-*sn*-glycero-3-phosphoinositol; TNP-PtdEtn, 2,4,6-trinitrophenyl-phosphatidylethanolamine; TIP3P, transferable intermolecular potential with 3-points.

tion, chylomicron retention disease, liver steatosis, and hypoglycemia in neonatal mice (12–14).

The biological importance of these proteins notwithstanding, PITPs remain poorly characterized with respect to how these proteins work as molecules. PITPs are not enzymes but proteins that mobilize energy-independent transfer of PtdIns and PtdCho between membranes *in vitro* (15, 16). On the basis of this operational assay, PITPs have historically been described to function as lipid carriers that transport PtdIns from its site of synthesis in the endoplasmic reticulum to the plasma membrane where agonist-stimulated phospholipase C-dependent pathways consume phosphoinositides, for which PtdIns is a metabolic precursor (16). An alternative mechanistic framework for thinking about how PITPs function as molecules is gaining strong momentum, however, and it conceptualizes a very different mechanism that does not involve intermembrane PtdIns transfer at all. Rather, PITPs are proposed to chaperone tightly channeled synthesis of privileged phosphoinositide pools dedicated to specific biological outcomes (17–19).

Regardless of whether PITPs function as PtdIns presentation modules or as *bona fide* PL-transfer proteins, there is no question that the PL-exchange reaction is central to their biological activity. The broad outline of the exchange reaction can be conceptualized by the PITP ejecting bound PL upon docking onto a membrane surface, followed by reloading of the PITP with another PL molecule prior to its disengagement from the surface. Studies in purified systems with defined liposomes and purified recombinant PITP demonstrate that abstraction of PL from a stable membrane bilayer during the exchange reaction occurs in the absence of any other co-factors or ATP (15, 16). Thus, PITPs somehow lower the activation energy of PL desorption from the bilayer, presumably by coupling protein conformational transitions to a cycle of PL unloading and loading. However, the fundamental details of the protein and PL dynamics associated with the exchange reaction are proving exceptionally challenging to dissect using conventional wet biochemistry approaches alone.

The first atomistic insights into the conformational dynamics associated with PL exchange were obtained from unrestrained molecular dynamics (MD) simulations and biochemical analyses of the major yeast PITP Sec14 (20). Although the MD time course was short (32 ns), oscillations between "open" and "closed" Sec14p conformers were simulated, and Sec14 structural elements were identified that control the conformational dynamics pathway associated with such oscillations. These included a flexible helical substructure that gates access to the PL binding pocket, a hinge region that supports helical gate motions, and a conformational switch element (the G-module) that couples gate dynamics with membrane/PL binding (20, 21). The Sec14 conformational circuitry described by those simulations is likely to be broadly conserved across the Sec14 protein superfamily, and available evidence makes the case that defects in this circuitry underlie inherited disease-associated mutations in mammalian Sec14-like proteins (20).

Although informative, those Sec14 simulations are limited. First, the MD simulations were conducted in the absence of a membrane bilayer. Thus, no information was forthcoming regarding PL–PITP interactions during the exchange reaction

(20). Fundamentally, it is those interactions that must be understood. Second, the detailed information gleaned from the Sec14 MD simulations does not translate to the vertebrate StART-domain PITPs, given that the two classes of PITPs are structurally unrelated. This issue takes on added force given the dramatic developmental and neurodegenerative phenotypes associated with genetic deficiencies in StART-domain PITP function in vertebrates and other metazoans (8–13). Addressing these major gaps in our knowledge for the first time, we report herein the protein and PL dynamics, and the free-energy landscape, of PtdIns and PtdCho exchange by the mammalian StART-domain PITPα.

Results

PITPα binding to the membrane bilayer

Both open apo-PITPα and closed PtdCho-bound holo-PITPα forms have been crystallized, and high-resolution structures have been solved (22, 23). The protein consists of four domains. The PL-binding cavity includes: (i) an eight-stranded β-sheet capped by two long α-helices; (ii) a regulatory loop speculated to be involved in mediating protein interactions; (iii) the C-terminal domain suggested to participate in closure of the PL-binding pocket; and (iv) a small lipid exchange loop speculated to form a lid over the PL-binding pocket and thereby gate access to it (Fig. 1A).

To examine the PITPα lipid exchange cycle at an atomistic level, extensive all-atom MD of both the open and closed PITPα conformers were run in systems reconstituted with bilayers consisting of PtdCho or PtdIns/PtdCho (supplemental Table S1). Root mean square deviation (RMSD) and root mean square fluctuation (RMSF) plots of PITPα Cα atoms showed that both conformers were stable during the simulations (Fig. 1, B and C). Higher flexibility was observed for the open conformer in the presence of the PtdCho/PtdIns membrane (Fig. 1B, *lower right panel*), and this was primarily accounted for by the increased flexibility of the PITPα extreme C terminus (Fig. 1C, *lower right panel*); that is, the substructure suggested to help gate access to the PITPα hydrophobic pocket.

The substructure bounded by residues 25–38 similarly exhibited enhanced flexibilities in the open conformer relative to the closed holo-PITPα. Indeed, it is in that former substructure that the most striking conformational change was observed during the MD. In all simulations involving the open PITPα conformer, the lipid exchange loop (bounded by residues 65–83) also transitioned from a turn in the starting structure into a 3_{10}-helical conformation during the MD simulation as evaluated by the DSSP (define secondary structure of proteins) algorithm that uses H-bond networks to classify secondary structure (24). In one simulation (system 4, open PITPα conformer), that conformational change coincided with insertion of the lipid-exchange loop into the bilayer upon PITPα association with the membrane.

To further characterize the stable and firm binding of PITPα to membrane, we used both theoretical and experimental data to define two criteria for identifying the most likely "on pathway" trajectories. First, trajectories that reported binding of the Trp[203]-Trp[204] motif to the membrane surface were considered
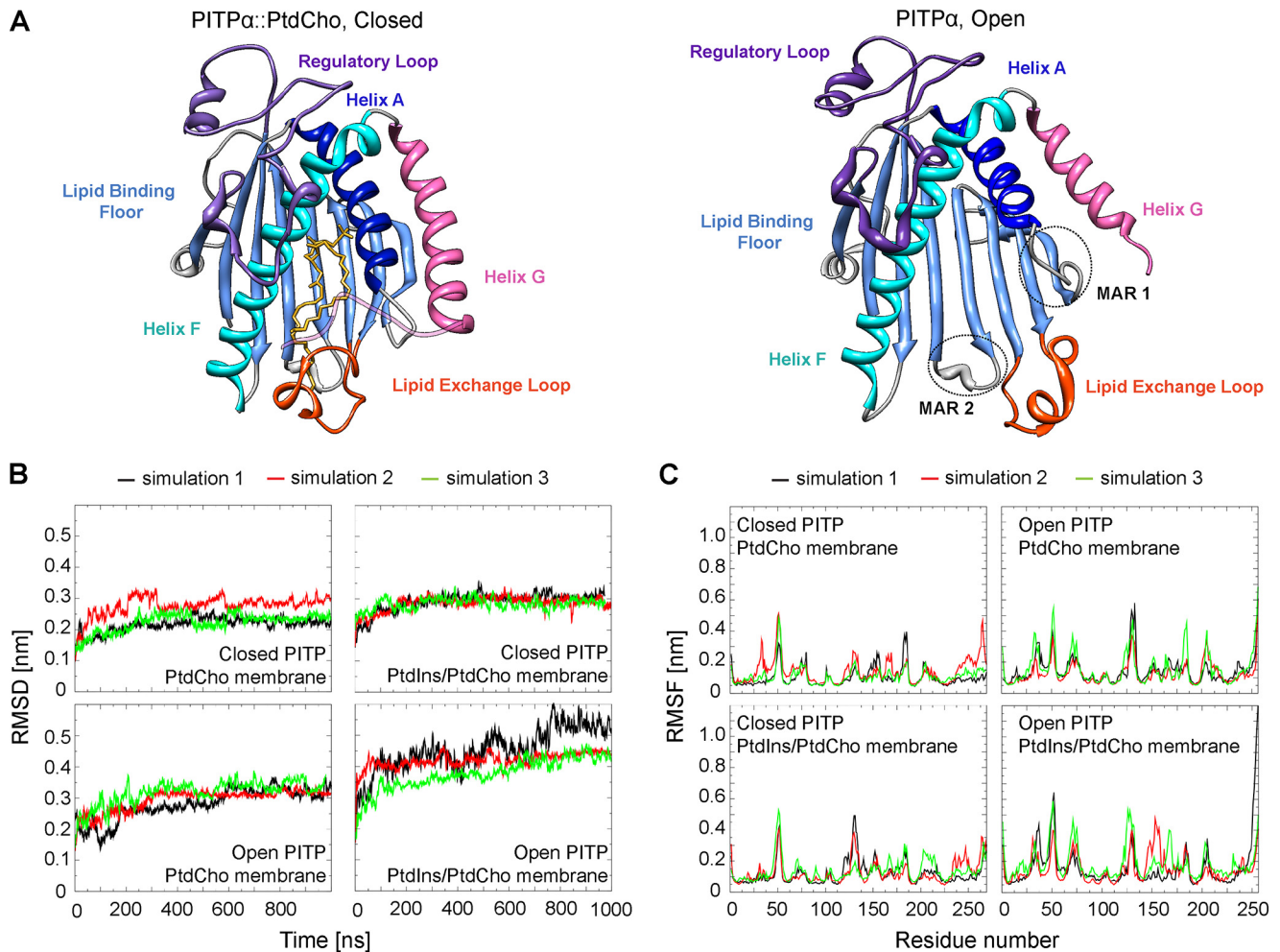
Figure 1. Molecular dynamics of PITPα on membranes. *A*, crystal structures of the closed PtdCho-bound PITPα conformer (PDB code 1T27) and the open apo-PITPα conformer (PDB code 1KCM) with substructures color-coded and labeled (*purple*, regulatory loop; *cornflower blue*, lipid binding floor; *dark blue*, helix A; *cyan*, helix F; *pink*, helix G; *orange*, lipid exchange loop). Membrane association regions identified by the MD simulations described in the text (MAR1, residues 28–41; MAR2, residues 99–110) are indicated with *dotted black circles* on the open PITP structure. *B*, RMSD of closed (*top panels*) and open (*bottom panels*) PITPα conformers in MD simulations on PtdCho (*left panels*) or PtdCho/PtdIns (*right panels*) bilayers. *C*, RMSF of open (*right panels*) and closed (*left panels*) PITPα conformers in MD simulations, on PtdCho (*top panels*) or PtdCho/PtdIns (*bottom panels*) bilayers. In each panel, analyses of each of three independent repeats are shown in different colors (*black*, simulations I; *red*, simulation II; *green*, simulation III).

to be on pathway given experimental evidence suggesting those residues to be important for membrane binding and lipid exchange by StART-like PITPs (25–27). Second, trajectories that were consistent with theoretical predictions from the Orientation of Proteins in Membranes (OPM) database (28), using PDB files for open and closed PITPα structures (PDB codes 1KCM and 1UW5, respectively), were also considered to be on pathway. Based on these criteria, we observed a firm and spontaneous PITPα binding to membrane in the following simulations: PtdCho/PtdIns membrane with closed PITPα repeats 1 and 2, PtdCho membrane with closed PITPα repeats 1 and 2, PtdCho/PtdIns membrane with open PITPα repeats 1 and 3, and PtdCho membrane with open PITPα repeats 1 and 3. Our discussion on the results and presentation of averaged data is based on these systems unless otherwise stated. Rationale for this choice can be viewed in supplemental Movies S1–S12, in which the residues Trp[203] and Trp[204] are depicted and were observed to undergo association with membrane. Moreover, the pattern of binding scored by the number of H-bonds established between protein and PL (supplemental Fig. S1A) was

consistent within these systems. Initial (0 ns) and final (1 μs) snapshots for all four representative simulations are presented in Fig. 2, and the time evolution of each membrane association event is documented in supplemental Movies S1–S12.

Detailed analyses of the occurrence of H-bond interactions between individual PITPα residues and PLs are compiled in supplemental Tables S2 and S3. Although the residues identified for membrane binding differed between the open and closed conformers in the PtdCho-only systems, some residues were consistently highlighted and identified three common regions involved in membrane association. Those regions were defined by: (i) the lipid exchange loop (residues 68–81), (ii) residues 135–163, and (iii) residues 204–220. With regard to specific interactions, Tyr[103] of the open conformer engaged the PtdIns/PtdCho membrane in hydrogen-bond interactions, whereas the C-terminal lid domain of the closed conformer (residues 259–264) interacted specifically with the PtdCho-only membrane. Parallel analyses in the PtdIns/PtdCho systems identified residues 147–153 and 208–219 in PITPα–PtdIns interactions (supplemental Table S3).
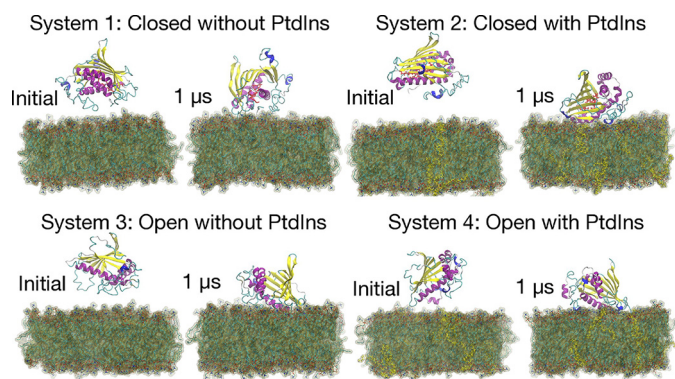
Figure 2. Association of PITPα with the membrane over the simulation time course. Shown are the initial (0 μs) and final (1 μs) snapshots from the simulations of systems: system 1 (closed PITP, membrane without PtdIns), system 2 (closed PITP, membrane with PtdIns), system 3 (open PITP, membrane without PtdIns), and system 4 (open PITP, membrane with PtdIns), as described in supplemental Table S1. The lipids are shown in *licorice* (PtdIns in *yellow* and PtdCho inside the binding pocket of PITP in *red*) and *transparent brown surface*. PITPα is rendered in new cartoon representation in colors corresponding to secondary structure (*yellow*, β-sheet; *purple*, α-helix; *blue*, 3_{10}-helix; *cyan*, random coil). Water molecules and ions are omitted for purpose of clarity.

Occurrence of contacts between PITPα and PL atoms were similarly monitored throughout the MD course where contact was set as an interatomic distance of ≤0.35 nm (supplemental Fig. S1B). Those analyses indicated that, in addition to the regions identified by H-bond analyses, both conformers showed that residues 28–41 constituted another membrane association region we term MAR1. Moreover, the open conformer uniquely presented one additional membrane association region we term MAR2 (residues 99–110), and this particular set involved interactions other than H-bonds (*e.g.* charge pairs). This unique membrane association area was able to interact with the bilayer surface because of the slightly different dock orientation of the open PITPα conformer on the membrane surface relative to that of the closed form, a difference that renders this protein region more accessible to the membrane for binding. For purposes of clarity, these MAR1 and MAR2 motifs are identified on the PITPα structure in Fig. 1A.

PITPα dynamics upon membrane association

After membrane binding, the closed PITPα molecule remained relatively inert throughout the remainder of the simulation. No unloading of bound PtdCho or opening of the lid was observed (supplemental Movies S1–S6). Specific conformational motions were observed upon membrane binding for the open PITPα conformer, however, and it is for this reason that focus was trained on this conformer. Interestingly, residues 25–38, implicated in membrane binding, exhibited enhanced mobility in the open form. Moreover, using the interatomic distance between residues Ser[30] and Glu[41] as a ruler for pocket closure, that distance decreased dramatically until it approached that observed in the closed conformer (Fig. 3 and supplemental Fig. S2).

The lipid exchange loop was also inserted into the cytoplasmic leaflet of the bilayer at this time where it underwent a transition from a turn to a 3_{10}-helix, as indicated by DSSP analysis, and adopted a more extended conformation as reported by
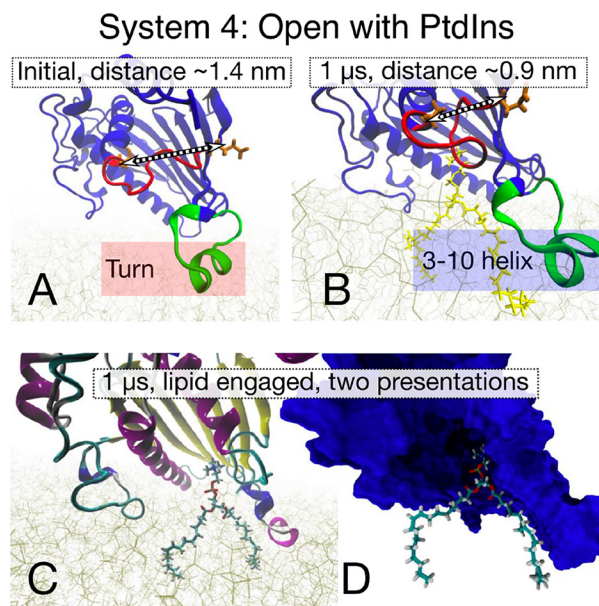

Figure 3. Conformational changes of PITPα during the simulation. *A* and *B*, initial (0 μs, *A*) and final (1 μs, *B*) snapshots from simulation system 4 using the open PITPα conformer as starting structure (supplemental Table S1). The loop consisting of residues 25–38 is depicted in *red*, residues Ser[30] and Glu[41] are in *orange licorice* representation, and the indicated distance between their Cα atoms is marked as a *dashed black double-headed arrow*. The lipid exchange loop is colored in *green*, and its conformational change between a turn (*red highlight*) and a 3_{10} helix (*blue highlight*) is indicated. The PtdCho lipid engaged by the lipid exchange loop is in *yellow licorice* representation. *C* and *D*, snapshots from simulation system 4 (as described in supplemental Table S1) of the open PITPα conformer in new cartoon representation (*C*) or *blue* surface representation (*D*), where a PtdCho molecule (in *licorice* representation) is engaged by the lipid exchange loop in the final (1 μs) step. Other lipids are shown as *brown sticks*, and water molecules and ions are omitted for clarity.

RMSF calculations (Fig. 1C) and by visual inspection (Fig. 3, *A* and *B*). Most interestingly, bilayer insertion of the lipid exchange loop (and the partial closure of the hydrophobic pocket) coincided with partial loading of a single PtdCho molecule into the open pocket (Fig. 3, *C* and *D*). We interpret the simulation data to conceptualize engagement of the lipid exchange loop with one PtdCho molecule with the result that the engaged PtdCho was extracted from the membrane bilayer and moved toward the hydrophobic pocket/water interface. PITPα was unable to consolidate those movements into vectorial transfer of PL into the hydrophobic pocket, however. Rather, the partially extracted PLs either slid back into the bilayer or engaged in bobbing movements at the cavity opening/water interface.

The role of PITPα residues Trp[203] and Trp[204] in the lipid exchange cycle is unclear. Several studies conclude that those residues are essential for lipid exchange by PITPα and closely related PITPs (25, 26), whereas other studies argue for minor roles for Trp[203] and Trp[204] in lipid exchange (27). Nonetheless, Trp[203] and Trp[204] were the first residues to interact with the lipid bilayer, and the Trp[203]–Trp[204] motif maintained interactions with membrane lipids throughout the MD time course. MD suggests that those Trp residues, and the residues that surround them, interact primarily with PtdIns (supplemental Fig. S1B).
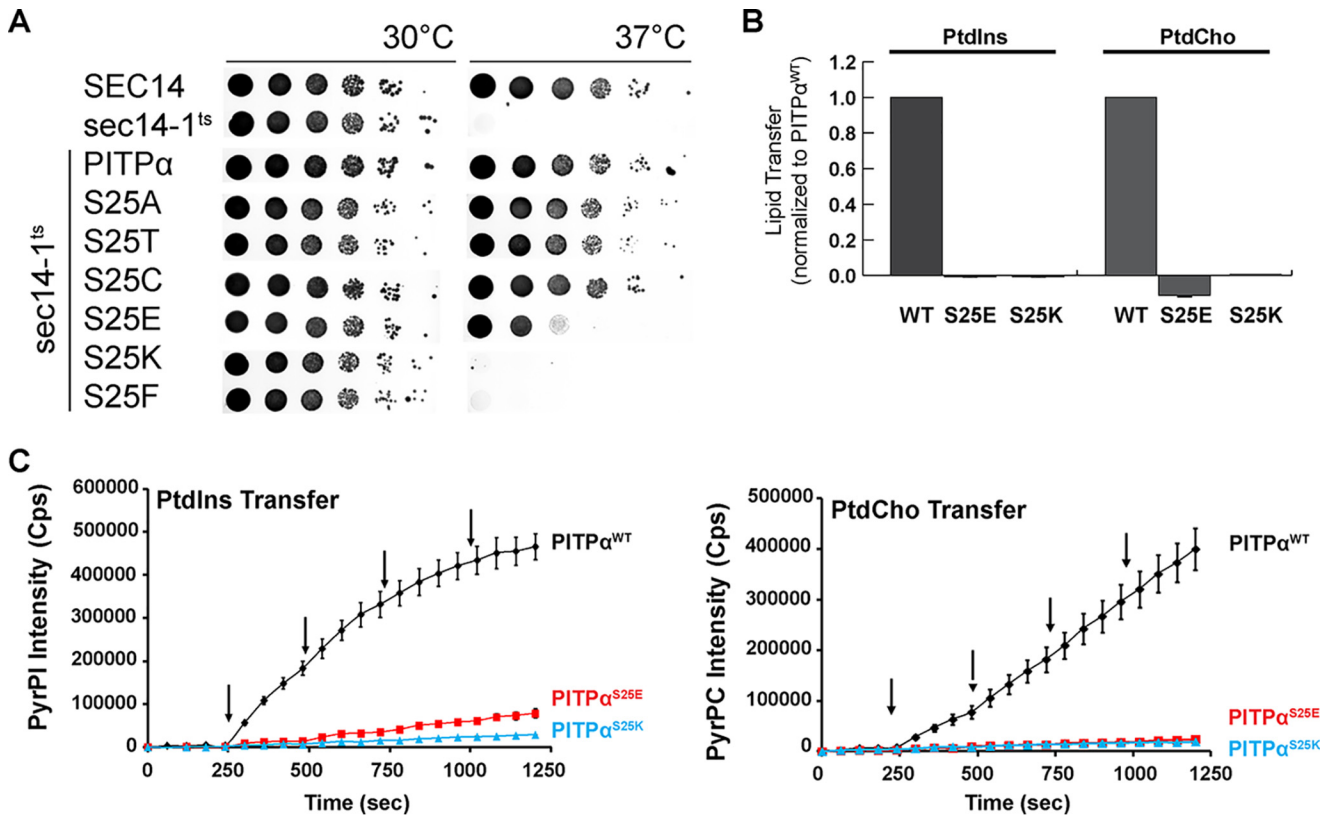
Figure 4. Functional consequences of missense substitutions for PITPα residue Ser[25]. *A*, phenotypic rescue assays. Isogenic *SEC14* (CTY182; *MATa ura3 -52, lys2-801, his3Δ200*) and *sec14-1[ts]* strains (CTY1-1A; *MATa ura3-52, lys2-801, his3Δ200, sec14-1[ts]*) served as positive and negative controls for PITPα activity, respectively. The latter strain fails to grow at 37 °C because activity of the major PITP is inactivated at that temperature (29). Isogenic *sec14-1[ts]* yeast strains carrying expression cassettes for *RnPITPNA*, or versions carrying the indicated substitutions for residue Ser[25], integrated at the *LEU2* locus, were spotted in 10-fold dilution series onto YPD agar plates and incubated at either permissive temperature of 30 °C or restrictive temperature of 37 °C for 48 h. *B*, end-point PtdIns and PtdCho transfer assays. Purified recombinant PITPα and indicated missense mutants (10 μg protein/assay) were assayed for [³H]PtdIns and [³H]PtdCho transfer, as indicated. Transfer efficiencies of PITPα were set at 100% (*n* = 3), and transfer of mutant PITPα proteins was normalized relative to PITPα activity values obtained from the same experiments. Assay efficiencies and backgrounds for these experiments are summarized in supplemental Table S5. *C*, rates of PyrPtdIns and PyrPtdCho transfer were measured for the indicated Ser[25] substitution mutants. Fluorescence intensities of PyrPtdIns or PyrPtdCho are plotted as a function of time. *Black arrows* mark addition of a 1-μg increment of the indicated protein. Following protein addition, the observed increase in fluorescence intensity was directly proportional to the relative transfer efficiency of the protein being assayed. The initial slope after each addition was calculated to obtain relative transfer efficiencies (supplemental Table S6). *Error bars* were calculated from two independent determinations.

Functional analyses of Ser[25] in PITPα activity

Residues 25–38 define a flexible region predicted to be involved in membrane binding, and the boundary residue Ser[25] is projected to be involved in H-bonding to PtdCho and PtdIns within the PITPα hydrophobic pocket. To assess the importance of Ser[25] to PITPα function, this residue was altered to Phe, Ala, Cys, Glu, Lys, and Thr. All mutant proteins were confirmed to be stable when expressed in yeast (supplemental Fig. S3). Mutant proteins were subsequently analyzed in *in vivo* and *in vitro* functional assays.

High-level expression of PITPα in yeast is sufficient to effect phenotypic rescue of the growth and membrane trafficking defects associated with temperature-sensitive mutations in the yeast *SEC14* gene (29), and this system enabled a general assessment of whether a mutant PITPα is functional or not. Expression of PITPα[S25A], PITPα[S25C], and PITPα[S25T] rescued *sec14-1[ts]*-associated growth defects at the restrictive temperature of 37 °C at an efficiency similar to that observed for PITPα (Fig. 4*A*). By contrast, PITPα[S25E] was only partially functional in this assay, whereas PITPα[S25F] and PITPα[S25K] scored as completely defective. Consistent with the *in vivo* results, purified recombinant PITPα[S25F] and PITPα[S25K] were also completely inactive

for PtdIns and PtdCho transfer *in vitro* in end-point assays using radiolabeled phospholipid substrates and a single clamped protein concentration (Fig. 4*B*). Thus, although some substitutions were tolerated for Ser[25], the functionality pattern did not correlate with H-bonding capacity (*e.g.* S25A scored as active). Rather, activity correlated best with the accessible surface area of the residue at that position. Residues compatible with efficient function (Ser, Ala, Cys, and Thr) have small accessible surface areas (80, 67, 104, and 102 Å², respectively); those that supported partial function have larger values (Glu, 138 Å²); and residues not tolerated had the largest side chains (Phe and Lys; accessible surface areas of 175 and 167 Å², respectively).

Real-time dequenching approaches were used as independent assays to separately monitor PtdCho- and PtdIns-transfer rates. In those assays, transfer was recorded as enhanced fluorescence of pyrene-labeled phospholipid as it was mobilized from quencher-loaded donor vesicles to quencher-free acceptor vesicles (see "Materials and Methods"). The significantly reduced initial rates of PtdCho and PtdIns transfer by PITPα[S25E] and PITPα[S25K] were recapitulated in those experimental systems (Fig. 4*C*). These assays were able to resolve a small amount of PtdIns-transfer capacity for PITPα[S25E], which

accounts for the modest ability of the mutant to rescue Sec14 deficiency *in vivo* (Fig. 4, *A* and *C*).

Free energies of PL loading/unloading by PITPα

The 1000-ns atomistic MD runs were of insufficient length to describe a complete PL loading/unloading half-cycle. Thus, suitable free-energy calculation methods were employed to study the energetics of PL loading/unloading by PITPα. A steered MD simulation approach was used to obtain a pathway for positioning of PtdCho and PtdIns within the PITPα-binding pocket through a short pulling simulation (see "Materials and Methods"). Once this regime yielded a PL-loaded conformer, the pulling constraints imposed on PL position were released, and subsequent trajectories were used to extract the windows for umbrella sampling simulations. Those umbrella sampling simulations were then analyzed with the weighted histogram analysis method (see "Materials and Methods"). Our selection of the force constant, together with the window spacing, provided sufficient sampling of the configuration space along the reaction coordinate as indicated by the satisfactory overlap of the histograms in supplemental Fig. S4*A*. Moreover, although each window was simulated for 40 ns, the obtained PMF stabilized within 10 ns of simulation, indicating that the free-energy profile converged to a stable value. We interpret this rapid convergence to reflect the fact that the starting structures for the umbrella sampling windows were extracted from unbiased trajectories. This interpretation follows previous demonstrations that the qualities of the starting structures for umbrella sampling have a significant impact on subsequent free-energy profile quality (30).

Because the exchange cycle occurs efficiently with purified PITPα and pure liposomes and without any ATP requirement, the activation energy for PL loading/unloading must be sufficiently low to be overcome by thermal fluctuations. Indeed, during the ensuing MD simulations (150 and 240 ns for the systems with PtdCho and PtdIns, respectively), bound PL was unloaded from the binding pocket and released into the bilayer (Fig. 5*A*). The PL unloading took place without any externally applied pulling forces. Taking advantage of these well equilibrated starting configurations, umbrella sampling simulations were extracted from the unloading trajectories, and the free energies related to PITPα interaction with PtdCho and PtdIns were calculated. The free-energy profiles for both PLs as a function of the distance along the bilayer normal are presented in Fig. 5*B*. Those profiles confirmed that PL loading into PITPα occurs within the realm of thermal fluctuation. The free energy of PtdCho uptake by PITPα was ~20 kJ mol^{-1} (8 k$_B$T), as calculated from the bottom of the global minimum to the maximum peak at 3 nm (Fig. 5*B*). The values for PtdCho and PtdIns desorption from the membrane bilayer were 90 and 120 kJ mol^{-1}, respectively (supplemental Table S4). The dramatic differences in the free energies of PL desorption in the presence *versus* absence of PITPα emphasize the remarkable role the protein plays in lowering the activation energy for that critical step.

For both PtdCho and PtdIns, the free-energy profiles identified two distinct minima. The first, at 1.5 nm, corresponded to the state where the PL was at equilibrium in the bilayer. The second was located in the membrane-distal region of the PL-binding cavity where the PL headgroups are coordinated by appropriate PITPα residues and the fatty acyl chains are incorporated into the most hydrophobic regions of the cavity. Unexpectedly, the free energies of loading for both PLs were similar, suggesting that the affinity of PITPα for PtdIns in the initial loading stage(s) was not appreciably higher than that for PtdCho. This was an unexpected outcome given crude estimates that PITPα has a 16-fold higher affinity for PtdIns than for PtdCho (15, 16). Another remarkable feature of the calculated free-energy profiles was that the minima at ~3.5 nm were very shallow. This property neatly accounts for why PL molecules that had partially loaded or were otherwise steered into the PITPα pocket were spontaneously and efficiently released into the bilayer via a reverse unloading reaction during simulation; that is, the energy barrier for unloading of bound PL is low.

PITPα–PL interactions within the hydrophobic pocket

Lipid–protein H-bond interactions within the PITPα hydrophobic pocket are likely required for serial consolidation of the loading reaction so that vectoriality is imposed on this process, which culminates in a complete loading reaction (*i.e.* rather than the reversible and futile partial loading reaction observed in the 1000-ns MD). Indeed, both PtdCho and PtdIns engaged in H-bonding within the PITPα-binding pocket, and the highest peaks in average H-bond interaction coincided with minima in the free-energy profiles (Fig. 5, *B* and *C*). Those results argued that H-bond interactions make critical contributions to the free-energy landscapes of the PtdCho and PtdIns loading/unloading reactions.

All pocket residues involved in H-bonding with PtdCho and PtdIns are highlighted in Fig. 5*C*. The unloading MD runs forecast that Lys[68] interacted primarily with PtdCho, whereas Thr[59], Lys[61], Glu[86], Asn[90], Thr[114], and Glu[218] interacted primarily with PtdIns. Satisfyingly, the former four residues were known from previous studies to engage PtdIns specifically (25, 31), whereas the latter two interactions represent new insights. Tyr[18], Gln[22], Ser[25], Tyr[63], Asn[101], Lys[195], and Gln[217] formed H-bonds with both PtdCho and PtdIns, and those residues had not previously been recognized to play any role in the PL-exchange cycle. The strong single H-bond interaction of Lys[68] with PtdCho was particularly noteworthy because it was observed early in the loading reaction sequence (supplemental Fig. S4*B*), suggesting that this previously unsuspected interaction plays a role in the PtdCho extraction process. PtdIns did not interact strongly with PITPα residue Lys[68]. Rather, it formed two H-bonds with Glu[218], another residue previously not suspected to play any role in lipid exchange (supplemental Fig. S4*B*). The MD projected that interactions of PtdCho and PtdIns with Lys[68] and Glu[218], respectively, defined the major contribution to peaks in the average H-bond plot at ~2.3 nm (Fig. 5*C*).

Functional analyses of Glu[218] and Lys[68] in PL transfer and binding

Lys[68] is a candidate residue for engaging PtdCho early in the PITPα-loading reaction. Structure-function experiments demonstrated PITPα^{K68E} or PITPα^{K68R} expression was less efficient

⑤ASBMB

J. Biol. Chem. (2017) 292(35) 14438–14455 **14443**
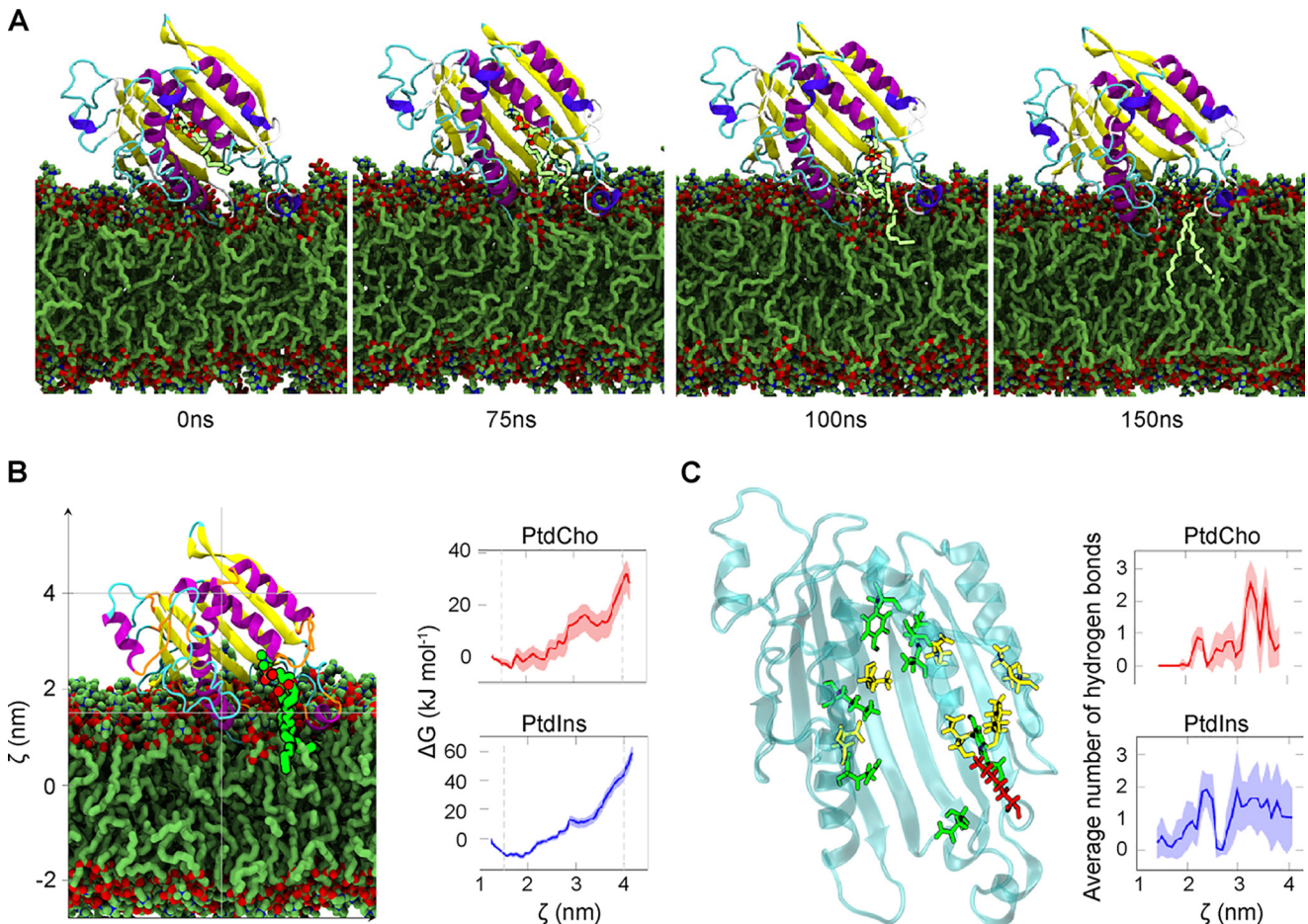
Figure 5. Steered molecular dynamics simulation of PL in the PITPα-binding pocket. Snapshots of the lipid unloading after the release of pulling force on the lipid (highlighted in *bright green*). *A*, individual panels correspond to ~0, ~75, ~100, and ~150 ns after the release of pulling force. Lipids are shown in *licorice*, and PITPα is shown in new cartoon representation. For purpose of clarity, water molecules and ions are not shown. *B, left panel*, snapshot from one of the umbrella sampling simulations windows showing PtdCho (*green VdW spheres*) being unloaded back into the membrane by PITPα (new cartoon representation). The *vertical axis* represents the reaction coordinate ζ (nm), where $\zeta = 0$ nm corresponds to the midplane of the lipid bilayer, and $\zeta = 2$ nm and $\zeta = 4$ nm correspond to the membrane-water interface and the upper part of the binding pocket, respectively. The *horizontal gray helplines* define the boundaries for lipid movement. *Right panel*, free-energy profiles for PtdCho (*red*) and PtdIns (*blue*) uptake/unload. *C, left panel*, PITPα and amino acid residues that form H-bonds with PtdCho and/or PtdIns. Residue projected to interact predominantly with PtdCho is depicted in *red* (Lys[68]), only with PtdIns in *yellow* (Lys[61], Glu[86], Asn[90], Thr[114], and Glu[218]), and in *green* residues that form H-bonds with both of the ligands (Tyr[18], Gln[22], Ser[25], Tyr[63], Asn[101], Lys[195], and Gln[217]). *Right panel*, average number of H-bonds interactions between PITPα and PtdCho (*red*) and PtdIns (*blue*), as indicated, as a function of time. Profiles are calculated as a function of the umbrella window, which has been translated into the reaction coordinate ζ (nm). The number of hydrogen bonds was calculated by counting all hydrogen bonds formed by a given residue, divided by the number of analyzed snapshots.

in phenotypic rescue of *sec14-1^ts*-associated growth defects relative to wild-type protein (Fig. 6A). Other substitutions were reasonably well tolerated as evidenced by PITPα[K68A], PITPα[K68C], and PITPα[K68Q] scoring as functional proteins in that assay. The biochemical properties of purified PITPα[K68E] were further examined in the end-point PtdCho and PtdIns transfer assays. Consistent with the predictions of the molecular dynamics simulation (MDS), PITPα[K68E] showed a ~70% reduction in PtdCho-transfer activity (Fig. 6B). However, the mutant PITP was also strongly defective in PtdIns-transfer, even though the MDS did not reveal strong interactions of Lys[68] residue with this PL. Real-time dequenching analyses confirmed the significantly reduced initial rates of PtdCho and PtdIns transfer and binding by PITPα[K68E] (Fig. 6, *C* and *D*).

Unlike Lys[68], residues Thr[114] and Glu[218] were scored to interact predominantly with PtdIns. Analyses of Thr[114] substitution mutants proved fruitless because the mutants were unstable proteins when expressed in yeast and, in all cases, the

mutant proteins quantitatively partitioned into inclusion bodies when expressed as recombinant proteins in *Escherichia coli*. Thus, our analyses focused on Glu[218], and this residue was of interest given that it was projected to form two H-bonds with PtdIns during the MD. Nonetheless, PITPα[E218A], PITPα[E218D], and PITPα[E218K] all scored as functional in the phenotypic rescue assay (Fig. 7A). Both end-point and real-time PtdIns and PtdCho transfer dequenching assays also showed that PITPα[E218A] was not significantly compromised for either PtdIns- or PtdCho-transfer activity (Fig. 7, *B* and *C*). However, the mutant protein was compromised for both PtdIns- and PtdCho-binding (Fig. 7D).

Functional analyses of Lys[195] in PtdIns and PtdCho transfer and binding

Lys[195] was highlighted in the MD simulations as a major contributor to the interaction of both PtdIns or PtdCho within the PITPα lipid-binding cavity (Fig. 8). Moreover, in indepen-
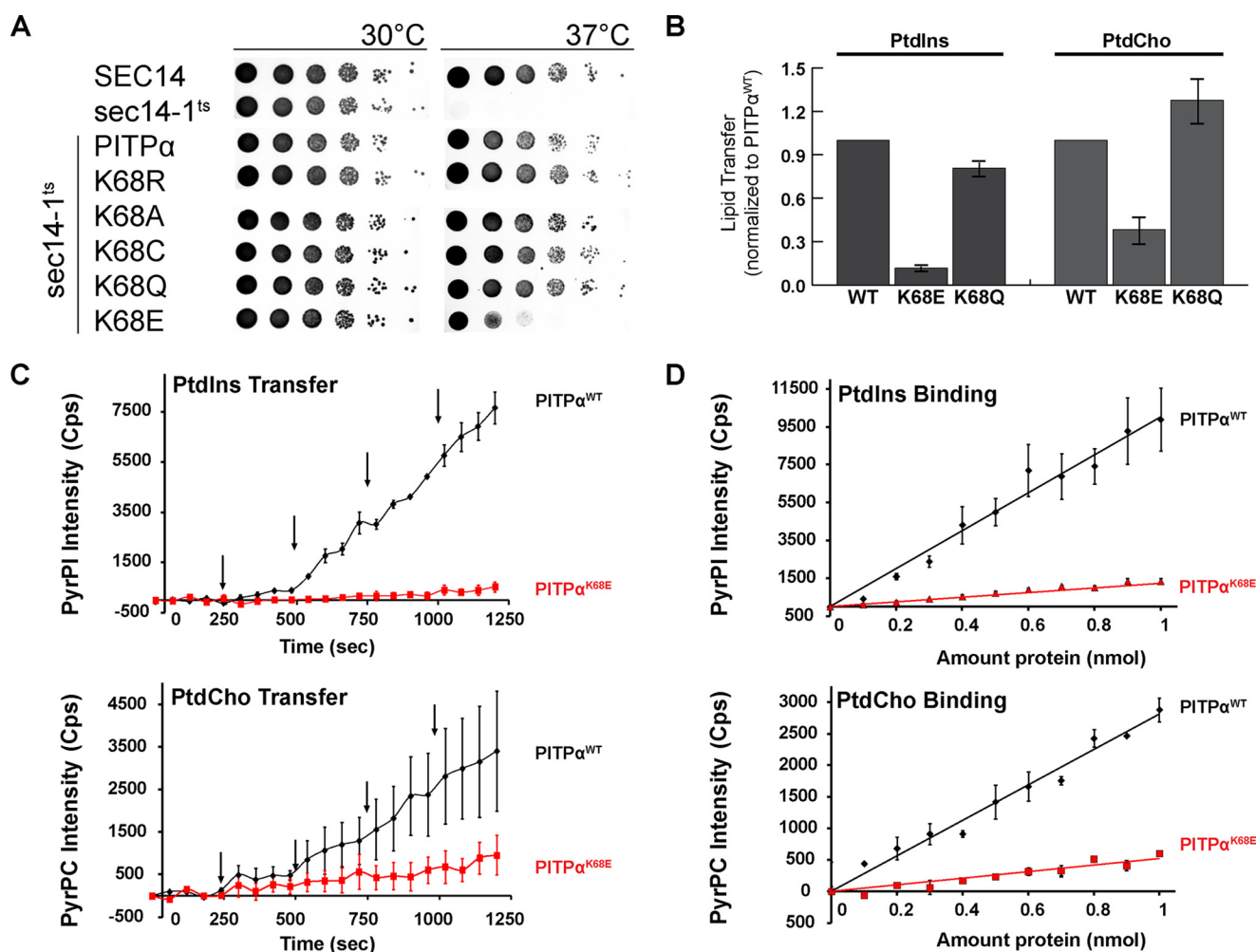
Figure 6. Functional consequences of missense substitutions for PITPα residue Lys[68]. *A*, details of the phenotypic rescue assays for mutant PITPα versions carrying the indicated substitutions for Lys[68] and the organization of this figure are described in the legend to Fig. 4*A*. *B*, end-point PtdIns and PtdCho transfer assays using purified recombinant PITPα and indicated missense mutants and organization of the figure are detailed in the legend to Fig. 4*B*. *C* and *D*, rates of PyrPtdIns and PyrPtdCho-transfer (*C*) and efficiencies of PyrPtdIns and PyrPtdCho-binding (*D*) were measured for the indicated Lys[68] substitution mutants. Experimental details are as described in Fig. 4*C*.

dent analyses, we serendipitously highlighted this same residue in a Cys-scanning mutagenesis screen on the basis of the 2.3 and 2.7 Å distance between Lys[195] and the phosphate moieties of bound PtdIns and PtdCho, respectively.[5] Thus, PITPα[K195C] was purified and analyzed with respect to PtdCho- and PtdIns-transfer rates and efficiencies of PtdCho and PtdIns binding (Fig. 8, *A* and *B*, respectively). PITPα[K195C] scored as nonfunctional in the yeast PITP activity assay because its expression was unable to rescue growth of *sec14[ts]* yeast mutants at 37 °C (Fig. 8*A*). PITPα[K195C] did not transfer PtdIns or PtdCho in the radiolabel transfer assay (Fig. 8*B*) and, as expected, was unable to transfer (Fig. 8*C*) or bind (Fig. 8*D*) pyrene-labeled PtdIns or PtdCho.

Conformational transitions of the PITPα C-terminal helix contribute to ligand specificity

PtdIns is the preferred exchange substrate for PITPα but the 1000-ns all-atom simulations of membrane-bound PITPα were

not informative regarding what headgroup-specific conformational transitions of the PITP might contribute to such ligand specificity. To understand how large conformational changes contribute to the ability of PITP to bind lipids, PITPα dynamics were simulated in a solvated system. In those simulations, the conformational transitions of apo-PITPα, the open PtdIns-bound conformer, and the open PtdCho-bound were compared. The latter two starting structures were generated by assigning PtdIns or PtdCho to their respective positions within the hydrophobic pocket as defined by X-ray crystallography (see "Methods and Materials"). MDS (250 ns) revealed conformational transitions from the open to the closed conformation.

Of relevance to this study, we focus on the C-terminal G-helix. Even though G-helix lies on the PITPα surface, and its side chains have no direct interaction with either PL (distance, >8 Å), this substructure exhibited differential dynamics in the 250-ns MD simulations depending on whether PtdIns or PtdCho was loaded into the open PITPα conformer. In both the open apo-PITPα and PITPα–PtdCho MDS, the G-helix remained stable, and no major uncoiling was observed (helix length average, 22 Å from Thr[240] to Asp[256]; Fig. 9*A*). This helix
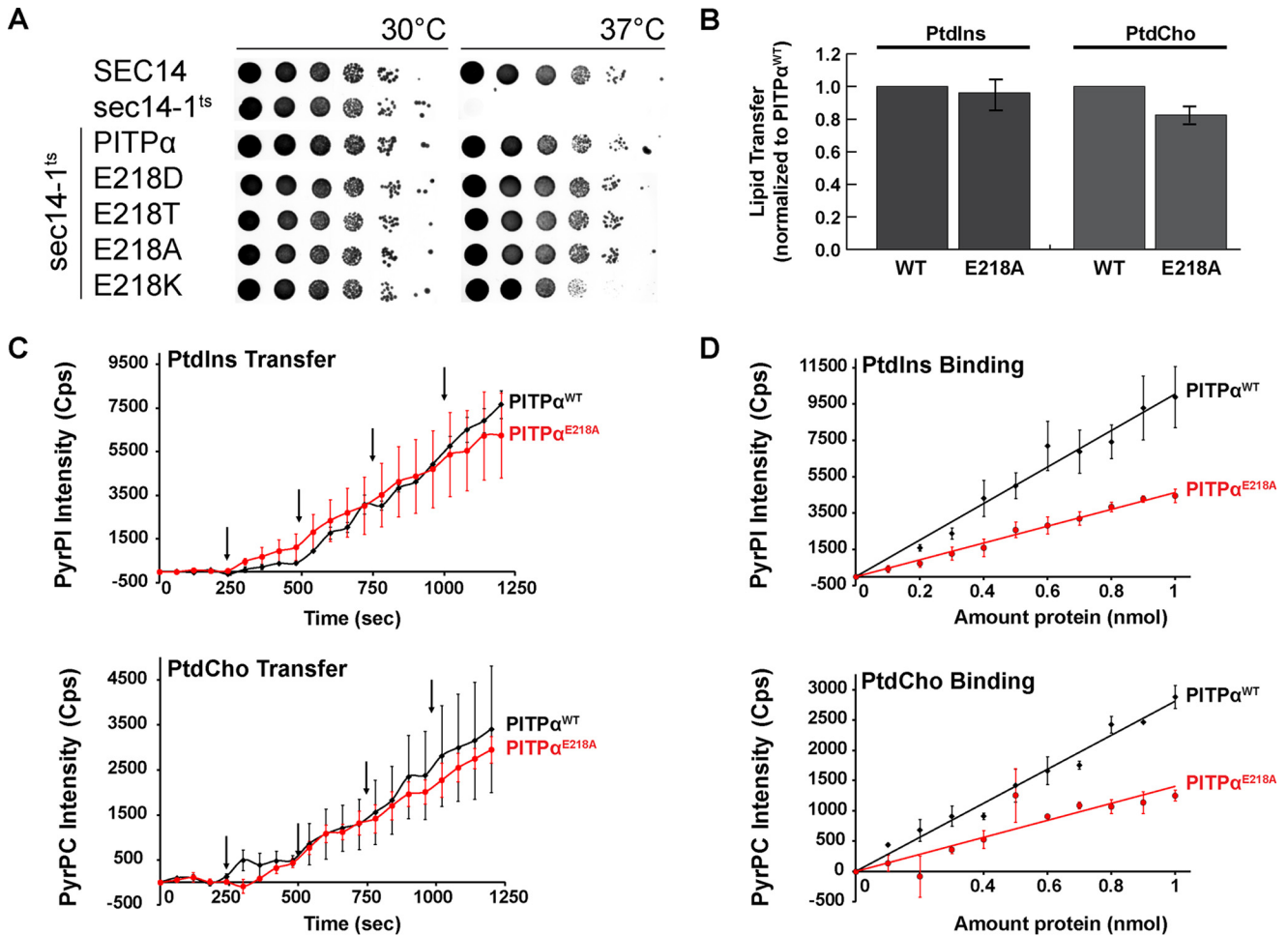
Figure 7. Functional consequences of missense substitutions for PITPα residue Glu[218]. *A*, details of the phenotypic rescue assays for mutant PITPα versions carrying the indicated substitutions for Glu[218] and the organization of this figure are described in the legend to Fig. 4*A*. *B*, end-point PtdIns and PtdCho transfer assays using purified recombinant PITPα and indicated missense mutants and organization of the figure are detailed in the legend to Fig. 4*B*. *C* and *D*, rates of PyrPtdIns and PyrPtdCho-transfer (*C*) and efficiencies of PyrPtdIns and PyrPtdCho binding (*D*) were measured for the indicated Glu[218] substitution mutants. Experimental details are as described in Fig. 4*C*.

underwent a conspicuous melting in systems modeling the open PITPα–PtdIns conformer, however (helix length average, 15 Å from Thr[240] to Glu[250]). Of note was a kinking of the helix at residue Glu[248], an invariant residue among the StART-like PITPs (Fig. 9*B*).

In the open PITPα–PtdCho conformer, the Glu[248] side chain was disposed to solvent on the G-helix surface and pointed away from the PtdCho headgroup. In that orientation, the side chain was in H-bond contact with G-helix residues Arg[245] and Lys[252] (both invariant StART-like PITP residues), thereby stabilizing the helical secondary structure. In the case of PITPα–PtdIns, however, Glu[248] was initially oriented toward the PtdIns headgroup. As the open PITPα–PtdIns conformer closed, however, the G-helix distorted, and the Glu[248] side chain twisted away from the PtdIns headgroup toward the protein surface. In that orientation, Glu[248] was primarily engaged in electrostatic interaction with Lys[252]. Residue Met[241] sits at the N-terminal end of the G-helix, and it too is invariant among the StART-like PITPs. Interestingly, Met[241] and Ile[244] (also highly conserved) engaged Leu[23] on the N-terminal A-helix via van der Waals interactions (Fig. 9*C*), suggesting an involvement for Met[241] and Ile[244] in stabilizing the A-helix. Those results offered a spe-

cific hypothesis for why the G-helix showed headgroup-specific dynamics given A-helix residues Tyr[18], Gln[22], and Ser[25] were identified as interacting with PtdIns and PtdCho in the 1000-ns MDS of membrane-bound PITPα.

Glu[248] and Met[241] execute specific functions in PtdIns transfer and binding

To determine whether the G-helix exhibits consequential headgroup-specific involvements in PITPα-mediated PL exchange, the functional properties of Glu[248] mutants were analyzed in detail. Indeed, missense substitutions at that position levied strong selectivity for PtdIns transfer and PtdIns binding relative to PtdCho binding/transfer. In the phenotypic rescue assay, only PITPα[E248D] showed activity, whereas PITPα[E248K], PITPα[E248A], and PITPα[E248T] all scored as strongly defective (Fig. 10*A*). The defects from the rescue assay were recapitulated in PtdIns-transfer assays, even though these mutant proteins retained wild-type abilities to transfer/bind PtdCho in end-point assays (Fig. 10*B*). PITPα[E248A] was also analyzed in the dequenching assay system where it again scored as completely defective for PtdIns transfer but showed essentially wild-type PtdCho-transfer activity (Fig. 10*C*). Those
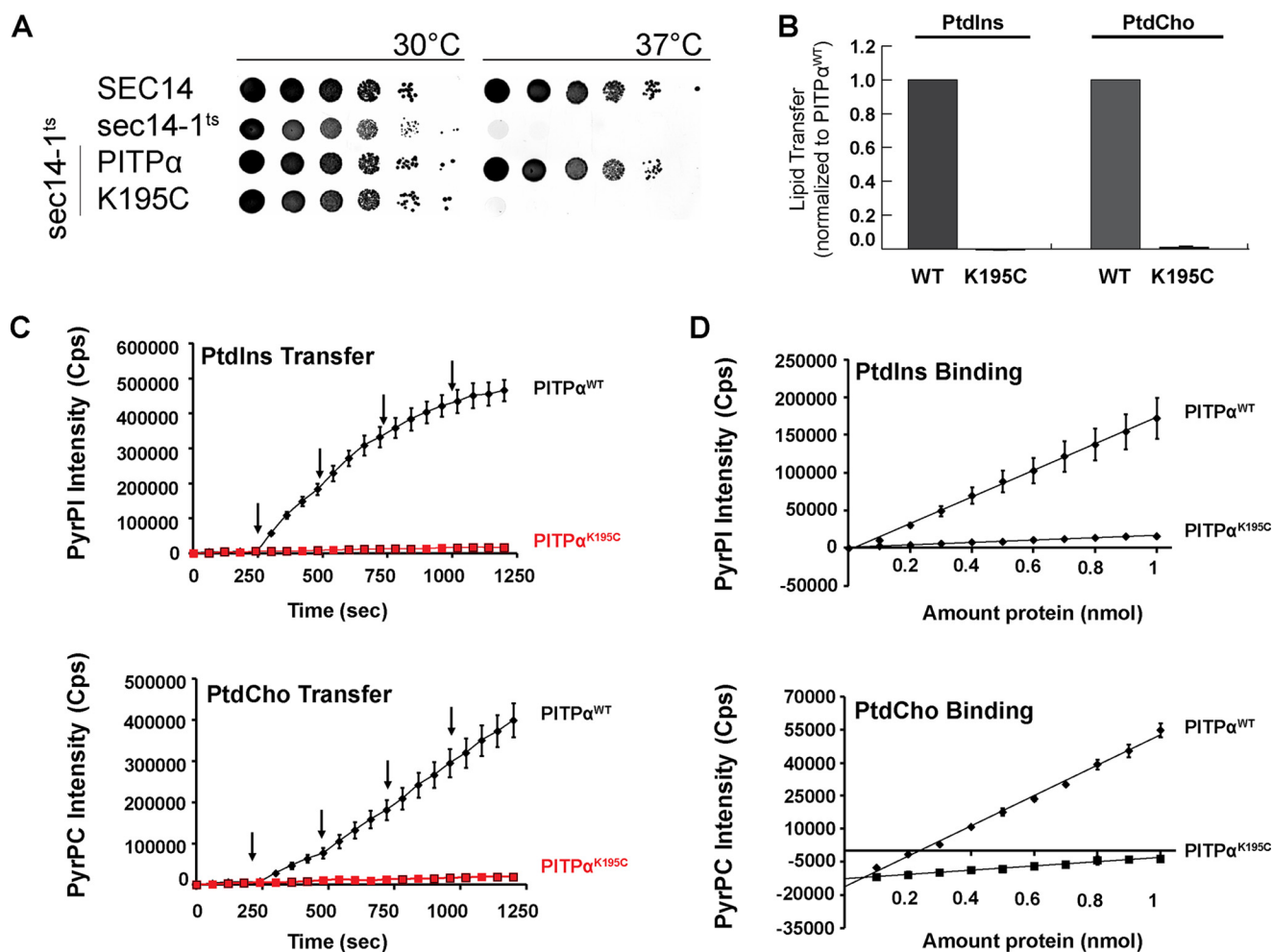
Figure 8. Functional consequences of missense substitutions for PITPα residue Lys[195]. *A*, details of the phenotypic rescue assays for mutant PITPα versions carrying the indicated substitutions for Lys[195] and the organization of this figure are described in the legend to Fig. 4*A*. *B*, end-point PtdIns and PtdCho transfer assays using purified recombinant PITPα and indicated missense mutants and organization of the figure are detailed in the legend to Fig. 4*B*. *C* and *D*, rates of PyrPtdIns and PyrPtdCho-transfer (*C*) and efficiencies of PyrPtdIns and PyrPtdCho binding (*D*) were measured for the indicated Lys[195] substitution mutants. Experimental details are as described in Fig. 4*C*.

headgroup-selective defects were further confirmed in real-time binding measurements for which PITPα[E248A] showed no PtdIns-binding activity in the time course of the assay while remaining fully competent for PtdCho binding (Fig. 10*D*).

The biochemical consequences of altering Met[241] were similarly analyzed. This residue was of particular interest not only for structural reasons as bridge between the G and A helices, but the M241T missense substitution is the consequence of a SNP circulating in the human population (32). As observed for the PITPα[E248A,K,T] mutants, PITPα[M241T] was selectively compromised for PtdIns-transfer activity. The mutant protein exhibited a 50% decrease of PtdIns-transfer activity with no diminution in its ability to transfer PtdCho (Fig. 10*B*).

Discussion

The PL-exchange cycles of PITPs are essential to their critical functions in stimulating the activities of PtdIns 4-OH kinases for biologically sufficient production of phosphoinositides (18). The basic form of this cycle, however, is not at all understood for any PITP. Herein, we describe a series of unrestrained MD simulations of mammalian PITPα that most likely modeled interfacial processes associated with the initial steps of PITPα

reloading with PL after ejection of a previously bound PL molecule. Moreover, the simulations supported first calculations of the free-energy landscape of PtdIns and PtdCho exchange by mammalian PITPα. Additional simulations of PITPα in membrane-free systems described conformational transitions that modulate the lipid exchange cycle in surprisingly long-range and lipid headgroup–specific ways. These collective studies report new insights into the initial stages of PL exchange by PITPα, describe H-bonding interactions between PL and protein within the PITPα hydrophobic pocket, and provide the first clues as to how PITPs lower the activation energy of PL desorption from the membrane bilayer.

PITPα binding to membrane surfaces

Both the closed and the open PITPα conformers spontaneously bound membrane surfaces in equilibrium MD simulations, and the binding events were stable and occurred in the course of relatively short time scales (~200 ns). Membrane binding consisted of three components. The first was direct interactions of the PITP with lipid at the membrane surface as counted by the number of H-bonds established between protein and PL. This component involved two separate regions
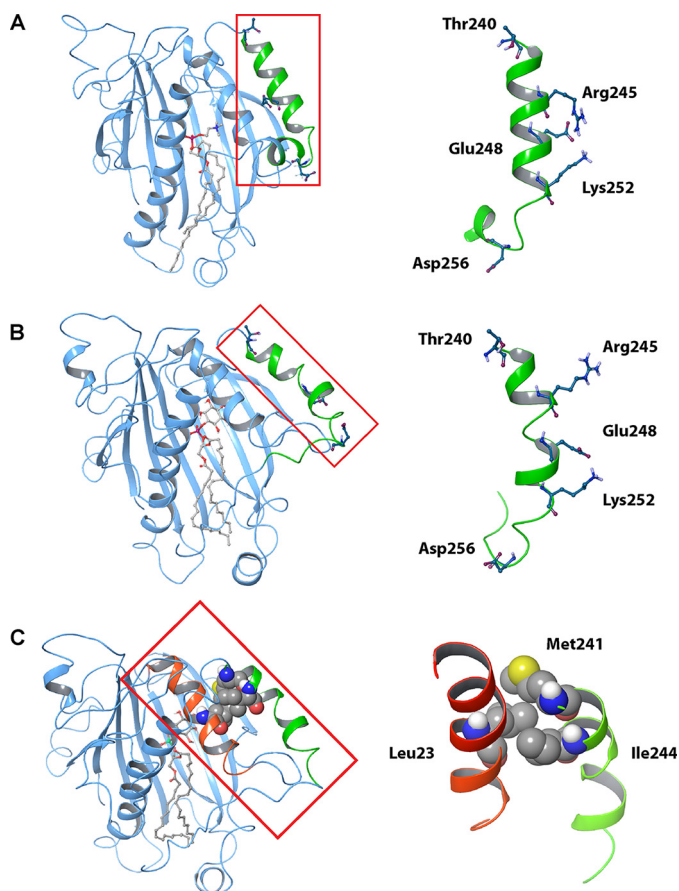
Figure 9. Molecular dynamics of PITPα open conformer G-helix in a solvent box. *A* and *B*, snapshots (110 ns) are shown from the MDS of PITPα–PtdCho (*A*) and PITPα–PtdIns (*B*). Blow-ups of the corresponding G-helices are shown to the *right* of the corresponding PITPα–PL structures. PITPα is illustrated in *blue ribbon* render with the G-helix shown in *green* and key residues shown in *stick* model. PtdCho and PtdIns are illustrated in *stick* render. *C*, simulated van der Waals interactions apparent at 110 ns of simulation of PITPα–PtdIns between G-helix residues Met[241], Ile[244], and the A-helix residue Leu[23] are shown. A magnified A-helix is shown in *orange*, and the G-helix is in *green* with interacting residues in CPK rendering at *right* of the PITPα–PtdIns structure.

bound by residues Lys[135]–Lys[163] and Trp[204]–Arg[220] as membrane-association domains. The second component was unique to the open PITPα conformer and involved a membrane insertion unit (the lipid exchange loop defined by residues Lys[68]–Ala[81]) that penetrated into the bilayer and initialized the first steps of the PL-loading reaction of the PITPα lipid exchange cycle. The third component described PITPα conformational transitions that accompanied membrane binding/insertion events. One of these motions involved lipid exchange loop (Lys[68]–Ala[81]) penetration into the bilayer. The other involved increased conformational flexibility and membrane association of residues Ser[25]–Glu[41]. The importance of this region to PITPα activity was confirmed by mutational analyses that were consistent with Ser[25] playing a key role in the conformational flexibility of this PITPα subdomain and this flexibility being required for PL exchange.

Initial steps of PL loading into apo-PITPα

The MD simulations predicted that a consequence of lipid exchange loop insertion into a mixed bilayer was a partial load-

ing of the open PITPα conformer with a single PtdCho molecule (at 700 ns in the simulation). This partial extraction of PtdCho from bilayer into the PITPα hydrophobic pocket was accompanied by a shielding of the fatty acyl chains from bulk membrane by the lipid exchange loop and partial closure of the unit that regulates accessibility to the lipid-binding pocket. Functional assays indicated amino acid substitutions in this substructure (*i.e.* for Lys[68]) compromised both PtdCho and PtdIns binding and exchange activities. It is now a both reasonable and attractive proposition that the inserted lipid exchange loop is the first protein substructure to interact with a PL molecule and that this interaction marks that PL molecule as a PITPα exchange ligand.

The progress in describing initial steps of the PL exchange cycle notwithstanding, we were unable to simulate full incorporation of PL into the PITPα lipid-binding pocket. Rather, the "chosen" PtdCho molecule entered a futile exchange reaction characterized by a shallow breathing conformational dynamics regime and ultimately fell back into the bilayer. Our interpretation is that the partially loaded PL encounters a free-energy well at an early step in the exchange cycle and that this barrier could not be negotiated during the 1000-ns simulation windows used in these experiments. Complete uptake of PL into the PITPα lipid-binding pocket requires extending simulation time scales sufficiently to allow additional conformational transitions to occur that direct the open PITPα from a shallow breathing regime to one that consolidates the PL-extraction process by supporting trajectories converging onto a closed conformer. An alternative, and not mutually exclusive, possibility is that the compositionally simple bilayers modeled themselves created a significant energy barrier that could not be negotiated during the 1000-ns MD. Natural membranes exhibit packing irregularities that might be productively exploited by the PITPα molecule in initiating a lipid exchange cycle, and such packing irregularities were minimal in the virtual bilayer systems analyzed in this study.

Free-energy landscape of PITPα interactions with lipid

Previous electron spin resonance studies rationalized the ATP independence of yeast Sec14-driven exchange cycle as a system where a PL molecule is engaged in a simple partitioning between two chemically similar microenvironments, *i.e.* the bilayer and the PITP PL-binding cavity (33, 34). The PITPα studies reported herein extend that concept. First, PITPα dramatically lowered the free energy of PL desorption from the bilayer to within the realm of thermal fluctuation. This lowering of an otherwise very significant thermodynamic barrier was driven by specific H-bond interactions between PITPα and lipid ligand headgroups.

Second, free-energy profiles for PtdIns and PtdCho trajectories through the lipid-binding pocket indicated that energy minima were shallow, thereby accounting for why PL molecules that had partially loaded, or were otherwise steered, into the PITPα pocket were spontaneously and efficiently released into the bilayer via a reverse unloading reaction during simulation. This feature likely reflects the fact that no larger conformational transitions of the PITP from the open to the closed state were observed in those 1000-ns simulations. Such conformational transitions would have the dual effects of dramatically
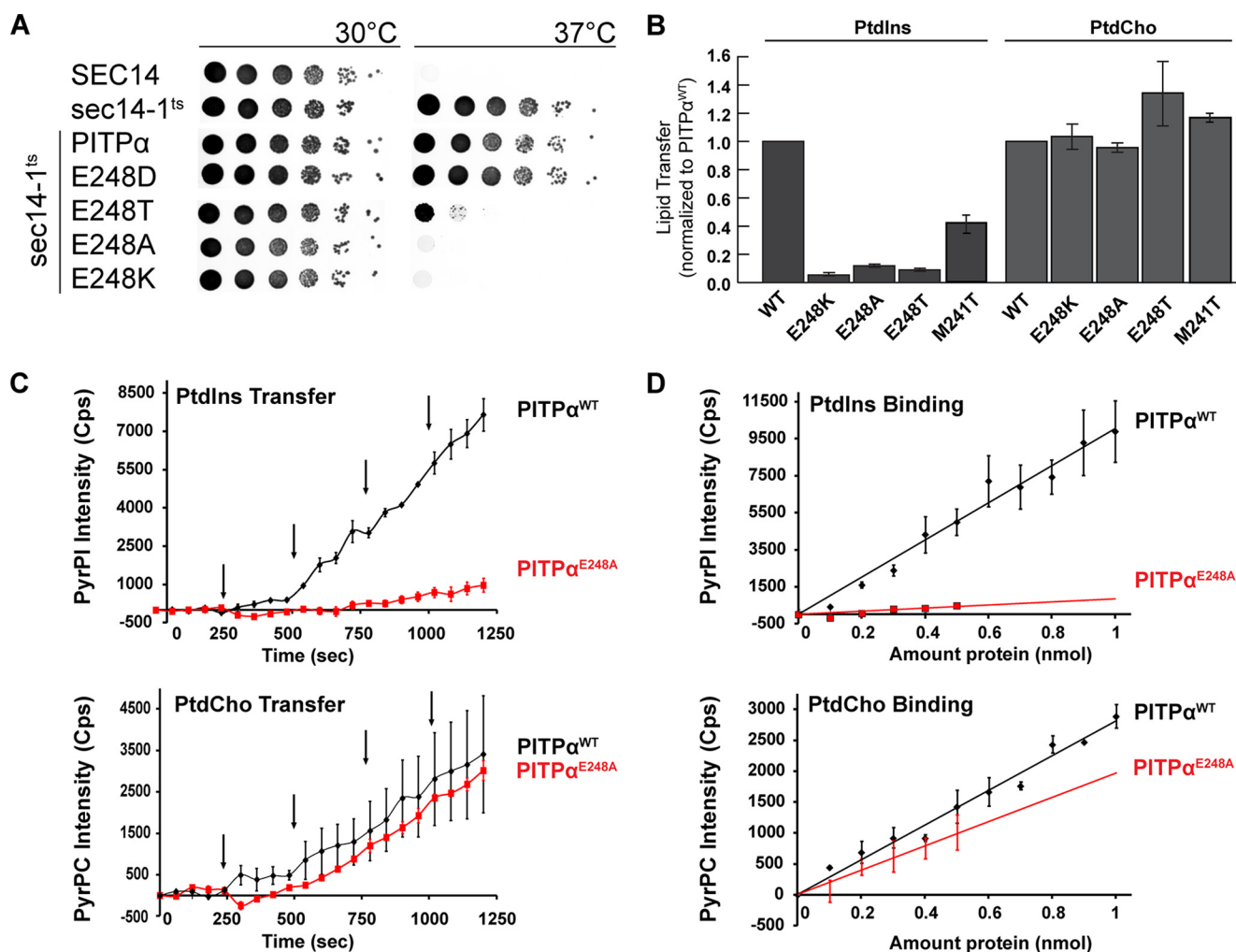
Figure 10. PtdIns-selective defects associated with missense substitutions for PITPα residue Glu[248] or Met[241]. *A*, details of the phenotypic rescue assays for mutant PITPα carrying the indicated substitutions for Glu[248] and the organization of this figure are described in the legend to Fig. 4*A*. *B*, end-point PtdIns and PtdCho transfer assays. Purified recombinant PITPα and indicated missense mutants and organization of the figure are detailed in the legend to Fig. 4*B*. *C* and *D*, rates of PyrPtdIns and PyrPtdCho-transfer (*C*) and efficiencies of PyrPtdIns and PyrPtdCho-binding (*D*) were measured for the indicated Glu[248] or Met[241] substitution mutants. Experimental details are as described in Fig. 4*C*.

impacting the free-energy landscapes of the exchange cycle and would likely contribute to the purported 16-fold greater affinity of PITPα for PtdIns *versus* PtdCho. Such a marked difference in PITPα affinity for PtdIns *versus* PtdCho was not at all apparent in our calculations because those analyses reported the free energies of loading for both PLs to be similar.

In support of this idea, a solvent box–based MDS system that does model larger conformational motions of the PITPα molecule indicated that headgroup-specific conformational transitions within the C-terminal G-helix exerted headgroup-specific control of the PL-exchange cycle. This finding is interesting for two reasons. First, the G-helix does not contact bound PtdIns or PtdCho directly and is far removed from both headgroups. Second, the M241T missense substitution in the G-helix selectively compromises PtdIns-transfer activity and represents a recognized SNP circulating in the human population.

PITP–PL interactions during the exchange cycle

Umbrella sampling data of PL "unloading" provided novel insights into which PITPα residues play direct roles in facilitat-

ing PtdIns and PtdCho transit through the PITPα lipid-binding pocket. Superposition of the structural elements and residues identified in this study to play important roles in the PITPα PL-exchange cycle, with primary sequences of other members of the StART-like PITP family, lend further confidence in the veracity of the data. MD simulations projected six residues of the PITPα lipid-binding pocket interact with PtdIns (Thr[59], Lys[61], Glu[86], Asn[90], Thr[114], and Glu[218]) and, of those, all but Glu[218] are absolutely conserved in evolutionarily distant members of the larger StART-like PITP family (Fig. 11). The one exception (Glu[218]) is invariant among evolutionarily distant class 1 StART-like PITPs. MD simulations also identified seven residues of the PITPα lipid-binding pocket as engaging both PtdIns and PtdCho in H-bond interactions (Tyr[18], Gln[22], Ser[25], Tyr[63], Asn[101], Lys[195], and Gln[217]). Of those, three are invariant (Tyr[18], Asn[22], and Lys[195]), one is invariant with a single exception involving a conserved substitution at that position (Tyr[63]), and two others are invariant among the class 1 StART-like PITPs from primates to flies (Ser[25] and Asn[101]; Fig. 11). This correspondence is remark-
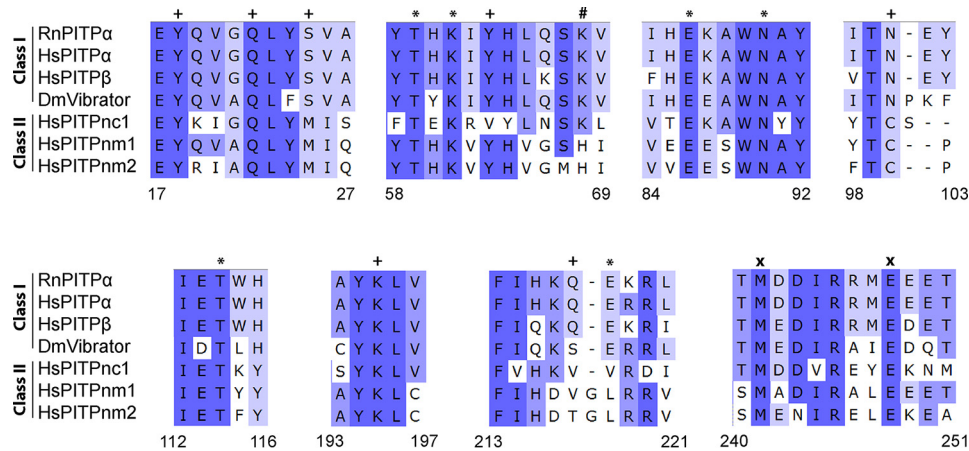
Figure 11. Primary sequence alignments of selected regions of class I and II StART-like PITPs. Sequences for PITP genes were extracted from the NCBI database using the following protein ascension numbers: RnPITPNA (NP_058927.1), HsPITPNA (NP_006125.1), HsPITPNB (NP_036531.1), DmVibrator (NP_524404), HsPITPNC1 (NP_858057), HsPITPNM1 (NP_004901.2), and HsPITPNM2 (NP_065896.1). For the multidomain PITPs HsPITPNM1 and HPITPNM2, only the PITP domain primary sequence is included in the alignment as guided by primary sequence homology to HsPITPα. Alignments were generated in VectorNTI using the AlignX module set to default parameters and visualized using UGENE. Indicated at the *bottom* for purposes of reference are residue numbers according the RnPITPα primary sequence. Color coding follows UGENE homology descriptors, where identical residues are on a *dark blue background*, non-similar residues are on a *white background*, and highly or weakly conserved residues fall in between on the *blue background gradient*. Residues predicted by MD to have predominantly PtdIns-specific interactions (*) include Thr[59], Lys[61], Glu[86], Gln[90], Thr[114], and Glu[218]; predominantly PtdCho-specific interactions (#) include Lys[68]; and interactions with both PtdIns and PtdCho (+) include Tyr[18], Gln[22], Ser[25], Tyr[63], Gln[100], Lys[195], and Gln[217]. Residues Met[241] and Glu[248] have specific roles in PtdIns transfer via a mechanism that does not involve direct phospholipid binding, and these residues are highlighted by (**X**) at top.

able given that MDSs are agnostic to experiment and to primary sequence alignments.

Of the set of identified specific interactions put to the functional test, the MD simulations were not absolutely accurate in their precise descriptions of headgroup-specific interactions. However, whereas the suggested lipid headgroup specificities were not borne out by experiment, the MD simulations did accurately identify these residues as important for optimal lipid exchange activity. The functional involvements of these residues in the exchange cycle were otherwise invisible to analyses of PITPα crystal structures alone.

If there are degrees of freedom for what residues are tolerated at these positions, why would those residues be so conserved across large evolutionary distances? We speculate that although there might be compensating interactions that are permissive for PL exchange in an *in vitro* system, strong evolutionary pressures are at play in cellular systems. For example, appropriate presentation of PtdIns to a PtdIns 4-OH kinase for biologically sufficient PtdIns-4-P production (*i.e.* in the face of cellular antagonists of PtdIns-4-P signaling) might demand stringent geometric requirements for PtdIns/PtdCho trajectories during the exchange cycle that are not apparent in *in vitro* lipid transfer assays.

Outstanding questions

Although the studies reported here describe the initial steps in a pathway of conformational transition from an apo-PITPα to a phospholipid-bound holo-PITPα and describe conformational transitions in the C-terminal G-helix that exhibit surprisingly long-range headgroup-specific involvements in the PL-exchange cycle, there remain outstanding considerations that will impact the details in important ways. First, the most productive MD simulations involved a membrane-docked PITPα conformer. At this point, it remains unknown how PL unloading is spatially or temporally related to PL loading. That is, are

these concerted processes, or are these separable reactions that proceed through an apo-PITPα intermediate? Although soluble probe accessibility experiments argue against the latter mode,[6] the MD simulations reported here do not and cannot explicitly consider concerted PL-loading/unloading exchange mechanisms. Whether the PL-loading and -unloading reactions are perfectly symmetrical processes also remains to be determined. Such symmetry is unlikely if PL-loading and unloading are concerted reactions. Finally, these simulations do not consider involvement of the PtdIns 4-OH kinase.

Those open questions notwithstanding, the satisfying congruence of the *in silico* data with the results of functional assays lends confidence that atomistic details of the PITPα PL-exchange reaction reported herein describe a reasonable first conceptualization of the initial stages of this key biological reaction. Extended MD production runs that capitalize on the membrane-docked apo- and holo-PITPα models described in this report now define promising approaches for linking the insights from the atomistic simulations of phospholipid loading/unloading by membrane-bound PITPα with insights culled from simulations of solvated PL-bound protein. We expect such extended simulations will extract new sets of fundamental mechanistic details regarding how the lipid-exchange cycle operates in StART-like PITPs.

Materials and methods

Atomistic molecular dynamics simulations

Molecular dynamics simulations were performed for PITPα in a system reconstituted with a lipid bilayer consisting of either pure PtdCho or a 90%/10% molar mixture of PtdCho and PtdIns. PITPα structures in the open (PDB code 1KCM) and closed (PDB code 1FVZ) conformations were retrieved from

---

the RCSB Protein Data Bank (22, 23). The former structure is lipid-free, whereas the latter describes PITPα in complex with a single bound PtdCho molecule. These two starting structures were each introduced into each of the two bilayer systems to generate a total of four distinct systems that were run in 1-μs all-atom simulations. The simulations were repeated three times for each system with different starting positions of the protein in water solution above membrane, together resulting in 3 μs of simulation time for each system and in overall 12 μs of simulation time. In all cases, PITPα was initially positioned above the bilayer in the water phase. Simulations were run at physiological salt concentrations (150 mM KCl), and counter ions were introduced to neutralize the total charge of the system. Details of the compositions of each simulated system are provided in supplemental Table S1.

The OPLS all-atom force field was used to describe all molecules (35). For water, the TIP3P model that is compatible with the OPLS parameterization was employed (36). The system structure used in this study is identical to those employed in our previous simulations of lipid bilayers (37, 38). To parameterize lipid molecules, parameters specifically derived for lipids were used (39–41). Periodic boundary conditions with the usual minimum image convention were employed in all three dimensions. The length of each hydrogen atom covalent bond was preserved by the LINCS algorithm (42). The integration time step was set to 2 fs, and the simulations were carried out at constant pressure (1 bar) and temperature (310 K). The temperature and pressure were controlled by the Parrinello–Rahman and velocity-rescale methods, respectively (43, 44). The temperatures of the solute and the TIP3P solvent were coupled separately. For pressure, a semi-isotropic scaling was employed. The Lennard–Jones interactions were cut off at 1.0 nm. For the electrostatic interactions, the particle mesh Ewald method (45) was employed with a real space cutoff at 1.0 nm, β-spline interpolation (sixth order), and a direct sum tolerance of 10^{-6}. The simulations were performed with the GROMACS 4.5.5 simulation package (46, 47).

Molecular dynamics simulations of PITP in a solvated system

Extensive (250 ns) MDS were carried out on PITPα structures prepared from the closed conformation bound to PtdCho (PDB code 1T27: 2.20 Å), the open conformation not bound to lipid (PDB code 1KCM: 2.00 Å), and the closed conformation complex with PtdIns (PDB code 1UW5: 2.20 Å). From these available crystal structures, several starting structures were generated in open conformation in combination with PtdCho and PtdIns. A total of 3 MD simulations were run for 250 ns each using the Desmond module of Schrodinger version 2016-3 (D. E. Shaw, Schrodinger Inc.), with the OPLS-AA forcefield as defined in Desmond. System Builder within Desmond/Schrodinger was used to generate a solvated system of protein-ligand complex. An orthorhombic box with a 12 Å buffer around protein–ligand complex was used to generate the periodic box. An all-atom atomistic scale MD simulation was carried out in a periodic box of explicit water molecules. For water, the TIP3P water model compatible with the OPLS-AA parameterization was employed. Simulation was carried out at 300 K at a physi-

ological salt concentration of 150 mM NaCl. Counter ions were included to neutralize the total charge of the system.

The OPLS-AA all-atom force field was used to describe all molecules, and the system was relaxed using Maestro's system relaxation protocol before the production run. That regime included a multistage relaxation protocol with two stages of minimization with 5000 steps of restrained minimization and 5000 steps of unrestrained minimization followed by five stages of MD runs with gradually diminishing restraints on solute-heavy atoms. These stages include 500 ps of restrained and 500 ps of unrestrained equilibration under an NVT ensemble. The system was further equilibrated under NPT ensemble with 300 ps of restrained equilibration, a 350 ps of restrained equilibration at 300 K with annealing off, and another 350 ps of unrestrained equilibration at 300 K. A separate MD production run of 250 ns was carried out at constant temperature and pressure.

Long-range electrostatic interactions were estimated using the particle mesh Ewald, whereas bonds involving protons were constrained using the SHAKE algorithm (48). A 2-fs time step was used throughout the simulation. The Thermostat Nose-Hoover chain method was applied with relaxation time of 1 ps (49). Barostat parameters were set according to Martyna *et al.* (50) with a relaxation time of 2.0 ps with isotropic coupling. A 9 Å cutoff was applied to Lennard–Jones interactions, and the nonbonded list was updated every 1.2 ps. The production run was continued for 250 ns, and snapshots of the coordinates were written out every 1 ps. The results were analyzed, and plots were generated within Maestro's simulation event analysis and simulation interaction diagram modules.

Free-energy calculations

Free energies of PtdCho and PtdIns uptake by PITPα were obtained by umbrella sampling simulations of two model systems. The starting structure of the first system was obtained from the final structure after a 1-μs production run of simulation 1 of the system composed of the open PITPα and PtdCho bilayer (supplemental Table S1, system 3). The second system was generated from the first by replacing the PtdCho molecule positioned closest to the binding site with a PtdIns molecule.

Free-energy profiles for PtdCho and PtdIns uptake by PITPα were calculated using the umbrella sampling method (51). The starting structures were obtained as follows. First, a single PL (PtdCho or PtdIns) was pulled from the bilayer toward the PITPα lipid-binding pocket along the z axis (membrane normal) in 20 ns of simulation with a constant pulling force constant of 1000 kJ $\times$ mol^{-1} $\times$ nm^{-2} and pulling rate of 0.00075 nm $\times$ ns^{-1} exerted on the lipid headgroup. Next, the position of the lipid headgroup was adjusted by lateral pulling such that it was positioned in the near vicinity of PITPα residues Cys[95] and Phe[225] reported to be important for PtdCho binding (22, 52) or residues Thr[59], Lys[61], Glu[86], and Asn[90] known to coordinate the inositol headgroup (25, 31). After the PLs were optimally positioned within the PITPα binding pocket, the constraints imposed on the respective headgroups were released. The PtdCho and PtdIns systems were then simulated for an additional 150 and 240 ns, respectively.

In umbrella sampling simulations, 28 and 26 windows with a spacing of 0.1 nm were employed for PtdIns and PtdCho sys-

tems, respectively. The reaction coordinate (ζ) was chosen as the z coordinate of the lipid headgroup with boundaries at the plane of the membrane-water interface and at the upper regions of the lipid-binding pocket. In each window, a harmonic restraining potential of 1000 kJ $\times$ mol^{-1} $\times$ nm^2 was applied in the z direction on the distance between the center of mass of the given headgroup and the PtdCho bilayer bound with PITPα. Finally, the free-energy profile for both PLs was constructed with the weighted histogram analysis method (53) based on the biased distribution of the given PL and magnitude of the umbrella biasing potential along the reaction coordinate. All free-energy calculations were performed with an identical set of simulation parameters as described above for the equilibrium simulations.

Visualization

All the snapshots and movies presented in this work were prepared using the VMD package (54). Molecular graphics and analyses of *Pitpna* single-nucleotide polymorphisms were performed with the University of California, San Francisco Chimera package developed by the Resource for Biocomputing, Visualization, and Informatics at the University of California, San Francisco.

Lipid reagents

For radiolabeled lipid transfer assays, preparation of [^{3}H] PtdIns rat liver microsomes has been described (1, 17). [^{3}H] PtdCho (L-α-dipalmitoyl [choline methyl-^{3}H], ART 0284) was purchased from American Radiolabeled Chemicals, Inc. For fluorescence-based lipid transfer assays, L-α-PtdCho and L-α-phosphatidic acid from chicken egg of highest available quality were purchased from Avanti Polar Lipids (Alabaster, AL) and used without further purification. 1-Palmitoyl-2-decapyrenyl-*sn*-glycero-3-phosphocholine (PyrPtdCho) was synthesized from 1-palmitoyl-2-hydroxy-*sn*-glycero-3-phosphocholine (Avanti Polar Lipids) and parinaroyl anhydride (55, 56) and purified by reverse phase HPLC chromatography (Beckman Ultrasphere ODS outfitted with 4.6 $\times$ 25-cm column (57)). 1-Palmitoyl-2-decapyrenyl-*sn*-glycero-3-phosphoinositol (PyrPtdIns) was prepared from yeast PtdIns and parinaroyl anhydride as described (58). 2,4,6-Trinitrophenyl-phosphatidylethanolamine (TNP-PtdEtn) was prepared as described (59) and purified by silica gel column chromatography. Stock solutions of lipids were prepared in methanol and kept at -20 °C. The concentrations of PyrPtdIns and PyrPtdCho were determined spectroscopically, whereas the concentrations of L-α-PtdCho, L-α-phosphatidic acid, and TNP-PtdEtn solutions were determined according to Rouser *et al.* (60). All lipid solutions were taken to ambient temperature before use. All other chemicals used were of highest available quality, and the organic solvents were of spectroscopic grade.

Yeast strains and media

Yeast were grown in YPD liquid medium (1% yeast extract, 2% bactopeptone, and 3% glucose), or SD liquid medium (0.67% nitrogen base, 3% glucose with appropriate amino acids supplemented) (61). The respective plate media included 2% agar. Yeast strains CTY182 (*MATa ura3-52 lys2-801 Δhis3-200*),

and CTY1-1A (*MATa ura3-52 lys2-801 Δhis3-200 sec14-1^ts^*) were previously described (1, 2, 62). *PITPNA*-expressing yeast strains were constructed by genomic integration of a single copy cassette where the *PITPNA* open reading frame was expressed under the control of the powerful and constitutive *PGK1* promoter (P_{PGK}) and configured in tandem with a functional *HIS3* selection marker. The integration cassette was recombined into the *LEU2* locus of the appropriate recipient yeast strain by standard lithium acetate transformation methods (62). Transformants were selected on media lacking histidine, and correct integration of the cassette was confirmed by screening for leucine auxotrophy as unselected phenotype. *PITPNA* overexpression strains were generated by transformation with the *PITPNA* expression cassette (driven by the powerful constitutive *PMA1* promoter) subcloned into a yeast *URA3* episomal plasmid pDR195 (63, 64). Transformants were selected on uracil-free medium.

Site-directed mutagenesis

The *Rattus norvegicus PITPNA* gene was mutated by site-directed mutagenesis in the P_{PGK1}-*PITPNA HIS3* yeast *LEU2* integration cassette, in the pDR195 (P_{PMA1}-*PITPNA*) vector, and in the pET28b-*His8-PITPNA* protein expression plasmid. Mutations were confirmed by DNA sequencing. Nucleotide sequences for primers the corresponding primers are available from the authors by request.

Protein purification

Recombinant PITPα and mutant versions were expressed from pET28b-*His8-PITPNA* vectors propagated in *E. coli* BL21 (RIL/DE3; New England BioLabs Inc., Ipswich, MA). Bacteria were cultured in 4 liters of TB + kanamycin/chloramphenicol medium for 4 h at 37 °C, shifted to 16 °C, and induced for recombinant protein expression with isopropyl β-D-thiogalactopyranoside (final concentration, 100 μM). The cultures were harvested after 18 h, and the cells were disrupted by passage through a French Press in low-phosphate lysis buffer (300 mM NaCl, 25 mM sodium phosphate, 5 mM 2-mercaptoethanol, pH 7.5). Clarified lysates were incubated with TALON metal affinity beads (Clontech), and bound proteins were step-eluted with imidazole (25–200 mM). Proteins were concentrated using the Amicon Ultra filter system (EMD Millipore), and concentration as determined by SDS-PAGE and comparison against a BSA standard mass series.

Lipid transfer assays

End-point assays measured transport of [^{3}H]PtdIns from rat liver microsomes to PtdCho liposomes or [^{3}H]PtdCho from liposomes (98 mol % PtdCho, 2 mol % PtdIns) to bovine heart mitochondria as described (1, 17).

PyrPtdCho and PyrPtdIns binding and transfer measurements were performed using a real-time dequenching assay as described by Somerharju *et al.* (65) with modification. For the transfer measurements, two vesicle populations were used. The donor (with TNP-PtdEtn quencher) and acceptor (without TNP-PtdEtn quencher) vesicles were prepared as follows. For the acceptor vesicles stock solutions of egg PtdCho and egg phosphatidic acid were mixed in a 291/9 nmol (97/3 mol %)

ratio and dried under a stream of N_2. The resulting lipid film was then hydrated with 2 ml of low phosphate buffer (25 mM Na_2HPO_4, 300 mM NaCl, pH 7.5) and sonicated on ice for 10 min. For the donor vesicles stock solutions of egg PtdCho, PyrPtdCho/PyrPtdIns, and TNP-PtdEtn were mixed in a 4/0.5/0.5 nmol ratio, solvent was evaporated, and the lipid film was resuspended in 10 μl of EtOH. The solution was injected into the buffer containing the acceptor vesicles. After a 5–10-min equilibrium period, the fluorescence intensity (excitation, 346 nm; emission, 378 nm) was measured as a function of time at 37 °C using a ISS K2 fluorimeter (ISS Inc., Champaign, IL).

To measure transfer from donor to acceptor, 1 μg of protein was injected every 250 s for a total of four injections. To obtain relative transfer efficiency, the initial slope after each protein injection was calculated, and the mean slope values for each protein ($n = 4$) was normalized to that calculated for purified PITPα. For binding measurements, donor vesicles were injected into 2 ml of low phosphate buffer. After a 5–10-min equilibrium period, the solution was titrated 10× with 0.1 nmol of recombinant protein, and fluorescence intensity was measured as a function of wavelength (excitation, 343 nm; emission, 360–450 nm) at 37 °C (K2 fluorimeter). The intensity at 348 nm was then plotted against protein amount, and the slope value for each protein was calculated and normalized against PITPα to obtain the relative binding efficiency.

Author contributions—A. G. and A. O. were involved in all aspects of the experimentation and experimental design, data analysis, manuscript preparation, and production of figures. A. T. was involved in all aspect of computational experimental design of the membrane-free MDS, data analysis, manuscript preparation, and production of figures. A. O., J. V., M. J., and T. R. designed and conducted MDS in bilayer-containing systems. A. G. and G. S. designed and performed the *in vivo* complementation experiments, and A. G. and M. L. designed and executed the *in vitro* lipid transfer and binding studies. P. S. synthesized the pyrene-labeled lipids used in this work. M. I. M. performed the mutant PITP stability assays. V. A. B. and I. V. were involved in all aspects of experimental design, data analysis, and manuscript preparation.

References

1. Bankaitis, V. A., Aitken, J. R., Cleves, A. E., and Dowhan, W. (1990) An essential role for a phospholipid transfer protein in yeast Golgi function. *Nature* **347,** 561–562
2. Cleves, A. E., McGee, T. P., Whitters, E. A., Champion, K. M., Aitken, J. R., Dowhan, W., Goebl, M., and Bankaitis, V. A. (1991) Mutations in the CDP-choline pathway for PL biosynthesis bypass the requirement for an essential PL transfer protein. *Cell* **64,** 789–800
3. Wu, W.-I., Routt, S., Bankaitis, V. A., and Voelker, D. R. (2000) A new gene involved in transport-dependent metabolism of phosphatidylserine, PSTB2/PDR17, shares sequence similarity with the gene encoding the PI-/PC-TP, Sec14p. *J. Biol. Chem.* **275,** 14446–14456
4. Ren, J., Lin, C. P., Pathak, M. C, Temple, B. R., Nile, A. H., Mousley, C. J., Duncan, M. C., Eckert, D. M., Leiker, T. J., Ivanova, P. T., Myers, D. S., Murphy, R. C., Brown, H. A., Verdaasdonk, J., Bloom, K. S., *et al.* (2014) A phosphatidylinositol transfer protein integrates phosphoinositide signaling with lipid droplet metabolism to regulate a developmental program of nutrient stress-induced membrane biogenesis. *Mol. Biol. Cell* **25,** 712–727
5. Vincent, P., Chua, M., Nogue, F., Fairbrother, A., Mekeel, H., Xu, Y., Allen, N., Bibikova, T. N., Gilroy, S., and Bankaitis, V. A. (2005) A Sec14p-nodulin domain phosphatidylinositol transfer protein polarizes membrane growth of *Arabidopsis thaliana* root hairs. *J. Cell Biol.* **168,** 801–812
6. Huang, J., Kim, C. M., Xuan, Y. H., Park, S. J., Piao, H. L., Je, B. I., Liu, J., Kim, T. H., Kim, B. K., and Han, C. D. (2013) OsSNDP1, a Sec14-nodulin domain-containing protein, plays a critical role in root hair elongation in rice. *Plant. Mol. Biol.* **82,** 39–50
7. Ghosh, R., de Campos, M. K., Huang, J., Huh, S. K., Orlowski, A., Yang, Y., Tripathi, A., Nile, A., Lee, H.-C., Schäfer, H., Dynowski, M., Róg, T., Lete, M. G., Ahyayauch, H., Alonso, A., *et al.* (2015) Sec14-nodulin proteins and the patterning of phosphoinositide landmarks for developmental control of membrane morphogenesis. *Mol. Biol. Cell* **26,** 1764–1781
8. Vihtelic, T. S., Hyde, D. R., and O'Tousa, J. E. (1991) Isolation and characterization of the *Drosophila* retinal degeneration B (rdgB) gene. *Genetics* **127,** 761–768
9. Milligan, S. C., Alb, J. G., Jr., Elagina, R. B., Bankaitis, V. A., and Hyde, D. R. (1997) The phosphatidylinositol transfer protein domain of *Drosophila* retinal degeneration protein B is required for photoreceptor cell survival and recovery from light stimulation. *J. Cell Biol.* **139,** 351–363
10. Giansanti, M. G., Bonaccorsi, S., Kurek, R., Farkas, R. M., Dimitri, P., Fuller, M. T., and Gatti, M. (2006) The class I PITP giotto is required for *Drosophila* cytokinesis. *Curr. Biol.* **16,** 195–201
11. Ile, K. E., Kassen, S., Cao, C., Vihtelic, T., Shah, S. D., Mousley, C. J., Alb, J. G., Jr., Huijbregts, R. P., Stearns, G. W., Brockerhoff, S. E., Hyde, D. R, Bankaitis, V. A. (2010) The zebrafish class 1 phosphatidylinositol transfer protein family: PITPα isoforms and double cone cell outer segment integrity in retina. *Traffic* **11,** 1151–1167
12. Hamilton, B. A., Smith, D. J., Mueller, K. L., Kerrebrock, A. W., Bronson, R. T., van Berkel, V., Daly, M. J., Kruglyak, L., Reeve, M. P., Nemhauser, J. L., Hawkins, T. L., Rubin, E. M., and Lander, E. S. (1997) The *vibrator* mutation causes neurodegeneration via reduced expression of PITPα: Positional complementation cloning and extragenic suppression. *Neuron* **18,** 711–722
13. Alb, J. G., Jr., Cortese, J. D., Phillips, S. E., Albin, R. L., Nagy, T. R., Hamilton, B. A., and Bankaitis, V. A. (2003) Mice lacking phosphatidylinositol transfer protein-α exhibit spinocerebellar degeneration, intestinal and hepatic steatosis, and hypoglycemia. *J. Biol. Chem.* **278,** 33501–33518
14. Alb, J. G., Jr., Phillips, S. E., Wilfley, L. R., Philpot, B. D., and Bankaitis, V. A. (2007) The pathologies associated with functional titration of phosphatidylinositol transfer protein α activity in mice. *J. Lipid Res.* **48,** 1857–1872
15. Helmkamp, G. M., Jr., Harvey, M. S., Wirtz, K. W., and Van Deenen, L. L. (1974) Phospholipid exchange between membranes. *J. Biol. Chem.* **249,** 6382–6389
16. Wirtz, K. W. (1991) Phospholipid transfer proteins. *Annu. Rev. Biochem.* **60,** 73–99
17. Schaaf, G., Ortlund, E. A., Tyeryar, K. R., Mousley, C. J., Ile, K. E., Garrett, T. A., Ren, J., Woolls, M. J., Raetz, C. R., Redinbo, M. R., and Bankaitis, V. A. (2008) The functional anatomy of PL binding and regulation of phosphoinositide homeostasis by proteins of the Sec14-superfamily. *Mol. Cell* **29,** 191–206
18. Bankaitis, V. A., Mousley, C. J., and Schaaf, G. (2010) The Sec14-superfamily and mechanisms for crosstalk between lipid metabolism and lipid signaling. *Trends Biochem. Sci* **35,** 150–160
19. Grabon, A., Khan, D., and Bankaitis, V. A. (2015) Phosphatidylinositol transfer proteins and instructive regulation of lipid kinase biology. *Biochim. Biophys. Acta* **1851,** 724–735
20. Ryan, M. M., Temple, B. R., Phillips, S. E., and Bankaitis, V. A. (2007) Conformational dynamics of the major yeast phosphatidylinositol transfer protein Sec14: insights into the mechanisms of PL exchange and diseases of Sec14-like protein deficiencies. *Mol. Biol. Cell* **18,** 1928–1942

ⓈASBMB

J. Biol. Chem. (2017) 292(35) 14438–14455 **14453**

21. Schaaf, G., Dynowski, M., Mousley, C. J., Shah, S. D., Yuan, P., Winklbauer, E. M., de Campos, M. K., Trettin, K., Quinones, M. C., Smirnova, T. I., Yanagisawa, L. L., Ortlund, E. A., and Bankaitis, V. A. (2011) Resurrection of a functional phosphatidylinositol transfer protein from a pseudo-Sec14 scaffold by directed evolution. *Mol. Biol. Cell* **22,** 892–905

22. Yoder, M. D., Thomas, L. M., Tremblay, J. M., Oliver, R. L., Yarbrough, L. R., and Helmkamp, G. M., Jr. (2001) Structure of a multifunctional protein. Mammalian phosphatidylinositol transfer protein complexed with phosphatidylcholine. *J. Biol. Chem.* **276,** 9246–9252

23. Schouten, A., Agianian, B., Westerman, J., Kroon, J., Wirtz, K. W., and Gros, P. (2002) Structure of apo-phosphatidylinositol transfer protein α provides insight into membrane association. *EMBO J.* **21,** 2117–2121

24. Kabsch, W., and Sander, C. (1983) Dictionary of protein secondary structure: pattern recognition of hydrogen-bonded and geometrical features. *Biopolymers* **22,** 2577–2637

25. Tilley, S. J., Skippen, A., Murray-Rust, J., Swigart, P. M., Stewart, A., Morgan, C. P., Cockcroft, S., and McDonald, N. Q. (2004) Structure-function analysis of phosphatidylinositol transfer protein α bound to human phosphatidylinositol. *Structure* **12,** 317–326

26. Yadav, S., Garner, K., Georgiev, P., Li, M., Gomez-Espinosa, E., Panda, A., Mathre, S., Okkenhaug, H., Cockcroft, S., and Raghu, P. (2015) RDGBα, a PtdIns-PtdOH transfer protein, regulates G-protein-coupled PtdIns(4,5)P$_2$ signalling during Drosophila phototransduction. *J. Cell Sci.* **128,** 3330–3344

27. Phillips, S. E., Ile, K. E., Boukhelifa, M., Huijbregts, R. P., and Bankaitis, V. A. (2006) Specific and nonspecific membrane binding determinants cooperate in targeting phosphatidylinositol transfer protein β-isoform to the murine *trans*-Golgi network. *Mol. Biol. Cell* **17,** 2498–2512

28. Lomize, M. A., Pogozheva, I. D., Joo, H., Mosberg, H. I., and Lomize, A. L. (2012) OPM database and PPM web server: resources for positioning of proteins in membranes. *Nucleic Acids Res.,* **40,** D370-D376

29. Skinner, H. B., Alb, J. G., Jr., Whitters, E. A., Helmkamp, G. M., Jr., and Bankaitis, V. A. (1993) Phospholipid transfer activity is relevant to but not sufficient for the essential function of the yeast SEC14 gene product. *EMBO J.* **12,** 4775–4784

30. Paloncýová, M., Berka, K., and Otyepka, M. (2012) Convergence of the free energy profile of coumarin in lipid bilayer. *J. Chem. Theory Comput.* **8,** 1200–1211

31. Alb, J. G., Jr., Gedvilaite, A., Cartee, R. T., Skinner, H. B., and Bankaitis, V. A. (1995) Mutant rat phosphatidylinositol/phosphatidylcholine transfer proteins specifically defective in phosphatidylinositol transfer: implications for the regulation of phosphatidylinositol transfer activity. *Proc. Natl. Acad. Sci. U.S.A.* **92,** 8826–8830

32. Lek, M., Karczewski, K. J., Minikel, E. V., Samocha, K. E., Banks, E., Fennell, T., O'Donnell-Luria, A. H., Ware, J. S., Hill, A. J., Cummings, B. B., Tukiainen, T., Birnbaum, D. P., Kosmicki, J. A., Duncan, L. E., Estrada, K., *et al.* (2016) Analysis of protein-coding genetic variation in 60,706 humans. *Nature* **536,** 285–291

33. Smirnova, T. I., Chadwick, T. G., MacArthur, R., Poluektov, O., Song, L., Ryan, M. M., Schaaf, G., and Bankaitis, V. A. (2006) The chemistry of PL binding by the *Saccharomyces cerevisiae* phosphatidylinositol transfer protein Sec14 as determined by electron paramagnetic resonance spectroscopy. *J. Biol. Chem.* **281,** 34897–34908

34. Smirnova, T. I., Chadwick, T. G., Voinov, M. A., Poluektov, O., van Tol, J., Ozarowski, A., Schaaf, G., Ryan, M. M., and Bankaitis, V. A. (2007) Local polarity and hydrogen bonding inside the Sec14 PL-binding cavity: high-field multifrequency studies. *Biophys. J.* **92,** 3686–3695

35. Jorgensen, W. L., and Tirado-Rives, J. (1988) The OPLS (optimized potentials for liquid simulations) potential functions for proteins, energy minimizations for crystals of cyclic peptides and crambin. *J. Am. Chem. Soc.* **110,** 1657–1666

36. Jorgensen, W. L., Chandrasekhar, J., Madura, J. D., Impey, R. W., and Klein, M. L. (1983) Comparison of simple potential functions for simulating liquid water. *J. Chem. Phys.* **79,** 926–935

37. Kaiser, H. J., Orlowski, A., Róg, T., Nyholm, T. K., Chai, W., Feizi, T., Lingwood, D., Vattulainen, I., and Simons, K. (2011) Lateral sorting in model membranes by cholesterol-mediated hydrophobic matching. *Proc. Natl. Acad. Sci. U.S.A.* **108,** 16628–16633

38. Orlowski, A., St-Pierre, J. F., Magarkar, A., Bunker, A., Pasenkiewicz-Gierula, M., Vattulainen, I., and Róg, T. (2011) Properties of the membrane binding component of catechol-*O*-methyltransferase revealed by atomistic molecular dynamics simulations. *J. Phys. Chem. B* **115,** 13541–13550

39. Maciejewski, A., Pasenkiewicz-Gierula, M., Cramariuc, O., Vattulainen, I., and Róg, T. (2014) Refined OPLS–AA force field for saturated phosphatidylcholine bilayers at full hydration. *J. Phys. Chem. B.* **118,** 4571–4581

40. Kulig, W., Pasenkiewicz-Gierula, M., and Róg, T. (2015) Topologies, structures and parameter files for lipid simulations in GROMACS with the OPLS-aa force field: DPPC, POPC, PtdCho, PEPC, and cholesterol. *Data Brief* **5,** 333–336

41. Kulig, W., Pasenkiewicz-Gierula, M., and Róg, T. (2016) Cholesterol interactions with *Cis* and *Trans* unsaturated phosphatidylcholines: molecular dynamics simulation study. *Chem. Phys. Lipids.* **195,** 12–20

42. Hess, B., Bekker, H., Berendsen, H. J. C., Fraaije, J. G. (1997) LINCS: A linear constraint solver for molecular simulations. *J. Comput. Chem.* **18,** 1463–1472

43. Parrinello, M., and Rahman, A. (1981) Polymorphic transitions in single crystals: a new molecular dynamics method. *J. Appl. Physics* **52,** 7182–7190

44. Bussi, G., Donadio, D., and Parrinello, M. (2007) Canonical sampling through velocity rescaling. *J. Chem. Phys.* **126,** 014101

45. Essmann, U., Perera, L., Berkowitz, M. L., Darden, T., Lee, H., and Pedersen, L. G. (1995) A smooth particle mesh Ewald method. *J. Chem. Phys.* **103,** 8577–8593

46. Hess, B., Kutzner, C., van der Spoel, D., and Lindahl, E. (2008) GROMACS 4: algorithms for highly efficient, load-balanced, and scalable molecular simulations. *J. Chem. Theory Comput.* **4,** 435–447

47. Pronk, S., Páll, S., Schulz, R., Larsson, P., Bjelkmar, P., Apostolov, R., Shirts, M. R., Smith, J. C., Kasson, P. M., van der Spoel, D., Hess, B., and Lindahl, E. (2013) GROMACS 4.5: a high throughput and highly parallel open source molecular simulation toolkit. *Bioinformatics* **29,** 845–854

48. Ryckaert, J. P., Ciccotti, G., and Berendsen, H. J. C. (1977) Numerical integration of the cartesian equations of motion of a system with constraints: molecular dynamics of *n*-alkanes. *J. Comp. Phys.* **23,** 327–341

49. Martyna, G. J., Klein, M. L., and Tuckerman, M. (1992) Nosé–Hoover chains: the canonical ensemble via continuous dynamics. *J. Chem. Phys.* **97,** 2635–2643

50. Martyna, G. J., Tobias, D. J., and Klein, M. L. (1994) Constant pressure molecular dynamics algorithms. *J. Chem. Phys.* **101,** 4177–4189

51. Kästner, J. (2011) Umbrella sampling. *Wiley Interdisciplinary Reviews: Comput. Mol. Sci.* **1,** 932–942

52. Garner, K., Hunt, A. N., Koster, G., Somerharju, P., Groves, E., Li, M., Raghu, P., Holic, R., and Cockcroft, S. (2012) Phosphatidylinositol transfer protein, cytoplasmic 1 (PITPNC1) binds and transfers phosphatidic acid. *J. Biol. Chem.* **287,** 32263–32276

53. Kumar, S., Rosenberg, J. M., Bouzida, D., Swenden, R. H., and Kollman, P. A. (1992) The weighted histogram analysis method for free-energy calculations on biomolecules: I. The method. *J. Comput. Chem.* **13,** 1011–1021

54. Humphrey, W., Dalke, A., and Schulten, K. (1996) VMD: visual molecular dynamics. *J. Mol. Graph.* **14,** 33–38

55. Selinger, Z., and Lapidot, Y. (1966) Synthesis of fatty acid anhydrides by reaction with dicyclohexylcarbodiimide. *J. Lipid Res.* **7,** 174–175

56. Gupta, C. M., Radhakrishnan, R., and Khorana, H. G. (1977) GlyceroPL synthesis: improved general method and new analogs containing photoactivable groups. *Proc. Natl. Acad. Sci. U.S.A.* **74,** 4315–4319

57. Patton, G. M., Fasulo, J. M., and Robins, S. J. (1982) Separation of PLs and individual molecular species of PLs by high-performance liquid chromatography. *J. Lipid Res.* **23,** 190–196

58. Somerharju, P., and Wirtz, K. W. (1982) Semisynthesis and properties of a fluorescent phosphatidylinositol analogue containing a cis-parinaoyl moiety. *Chem. Phys. Lipids* **30,** 81–91

59. Gordesky, S. E., and Marinetti, G. V. (1973) The asymmetric arrangement of PLs in the human erythrocyte membrane. *Biochem. Biophys. Res. Commun.* **50,** 1027–1031

60. Rouser, G., Fkeischer, S., and Yamamoto, A. (1970) A two dimensional thin layer chromatographic separation of polar lipids and determination of PLs by phosphorus analysis of spots. *Lipids* **5,** 494–496

61. Sherman, F., Fink, G. R., and Hicks, J. B. (1983) *Methods in Yeast Genetics*, Cold Spring Harbor Laboratory, Cold Spring Harbor, NY

62. Bankaitis, V. A., Malehorn, D. E., Emr, S. D., and Greene, R. (1989) The *Saccharomyces cerevisiae SEC14* gene encodes a cytosolic factor that is required for transport of secretory proteins from the yeast Golgi complex. *J. Cell Biol.* **108,** 1271–1281

63. Gietz, R. D., and Woods, R. A. (2002) Transformation of yeast by lithium acetate/single-stranded carrier DNA/polyethylene glycol method. *Methods Enzymol.* **350,** 87–96

64. Rentsch, D., Laloi, M., Rouhara, I., Schmelzer, E., Delrot, S., and Frommer, W. B. (1995) NTR1 encodes a high affinity oligopeptide transporter in *Arabidopsis. FEBS Lett.* **370,** 264–268

65. Somerharju, P. J., van Loon, D., and Wirtz, K. W. (1987) Determination of the acyl chain specificity of the bovine liver phosphatidylcholine transfer protein: application of pyrene-labeled phosphatidylcholine species. *Biochemistry* **26,** 7193–7199